

Journal of Iberian Geology

The importance of sequential partial melting and fractional crystallization in the generation of syn-D3 Variscan two-mica granites from the Carrazeda de Ansiães area, northern Portugal --Manuscript Draft--

Manuscript Number:	JIBG-D-20-00067R2	
Full Title:	The importance of sequential partial melting and fractional crystallization in the generation of syn-D3 Variscan two-mica granites from the Carrazeda de Ansiães area, northern Portugal	
Article Type:	S.I. : New developments in Geochemistry. A tribute to Carmen Galindo	
Funding Information:		
Abstract:	EU SOCFAC facility (HPRI-1999-CT-00108)	Dr. Rui José dos Santos Teixeira
	PhD grant from FCT - Fundação para a Ciência e a Tecnologia, Portugal (SFRH/BD/17246/2004)	Dr. Rui José dos Santos Teixeira
	Pole of the Geosciences Centre (CGeo) through FCT - Portuguese Foundation for Sciences and Technology (Projects UIDB/00073/2020 and UIDP/00073/2020)	Dr. Rui José dos Santos Teixeira
<p>At Carrazeda de Ansiães region, northern Portugal, a mesozonal granitic suite intruded Precambrian to Ordovician metasedimentary rocks during the late kinematic stages of the Variscan orogeny. In this multiphase granitic complex, consisting of ten granite types, the youngest group of two-mica granites (G7 - G10) was emplaced between 318 ± 1 Ma and 316.2 ± 0.7 Ma, as determined by ID-TIMS U-Pb on zircon and monazite. Granite types G7 - G9 were affected by the third phase of deformation (D3) before they were completely crystallized, as indicated by their internal NW-SE magmatic foliation concordant with the regional metasedimentary structures. The granite type G10 shows some distinctive textural features, showing a strong brittle deformation, probably due to its preferential emplacement in late NNE-SSW fault zones.</p> <p>Granites G7 - G9 have equal or higher amounts of muscovite than biotite and contain surmicaceous enclaves, xenoliths, "schlieren", and, more rarely, microgranular enclaves. The muscovite-dominant granite G10 does not contain enclaves. These Variscan granites are peraluminous, with ASI ranging between 1.22 and 1.39 and normative corundum of 2.79 – 4.39 %, having the characteristics of S-type granites. In fact, the enrichment in LREE relatively to HREE, the negative Eu anomalies, and similar mean values of $(87\text{Sr}/86\text{Sr})_i$, ϵ_{Nd} and $\delta^{18}\text{O}$ for G7 (0.7156 ± 0.0005; – 8.5; 11.49 ‰) and G8 (0.7155 ± 0.0007; – 8.4; 11.39 ‰) show that these two granite types resulted from sequential partial melting of the same metasedimentary material, where granite G8 would have derived from a higher degree of partial melting than G7.</p> <p>Granites G8-G10 and their minerals show a fractionation trend that is confirmed by modeling of major and trace elements. The subparallel REE patterns and the decreasing REE contents within the differentiation series, the Rb-Sr isochron for G8, G9 and G10 (315.5 ± 5.4 Ma; MSWD = 1.3) and the relatively uniform ϵ_{Nd} and $\delta^{18}\text{O}$ data suggest that fractional crystallization was the main mechanism, which would have lasted less than 1 Ma. The tin-bearing granites G7 and G10 have ≥ 20 ppm Sn, but the main quartz veins containing cassiterite and wolframite cut granite G10, which contains 31 ppm Sn. Fractional crystallization was responsible for the increase in Sn content in granites from the G8 - G10 series and their micas.</p> <p>En la región de Carrazeda de Ansiães, norte de Portugal, rocas metasedimentarias de edad Precámbrico y Ordovícico han sido intruidas por una suite granítica mesozonal durante las etapas tardí-cinemáticas de la orogenia Varisca. En esta suite se distinguen diez tipos de granito, de los que los más jóvenes, constituidos por granitos de dos micas (G7 - G10), se emplazan entre 318 ± 1 Ma y 316.2 ± 0.7 Ma, de acuerdo con dataciones U-Pb ID-TIMS en circon y monacita. Los granitos G7 - G9 han sido afectados por la tercera fase de deformación (D3) antes de su consolidación completa, como sugiere su foliación magmática interna NW-SE concordante con las estructuras metasedimentarias regionales. El granito G10 tiene algunas características texturales distintivas, propias de una fuerte deformación frágil, probablemente debidas a su</p>		

	<p>emplazamiento preferente en zonas de fallas tardías con dirección NNE-SSW. Los granitos G7 - G9 tienen cantidades de moscovita iguales o mayores que las de biotita y contienen enclaves "surmicaceous", xenolitos, "schlieren" y, raras veces, enclaves microgranudos. El granito G10 predominantemente moscovítico no contiene enclaves. Estos granitos variscos son peralumínicos, con valores de ASI entre 1.22 y 1.39, y de corindón normativo entre 2.79 – 4.39%, y presentan características típicas de granitos de tipo S. De hecho, el enriquecimiento en LREE con respecto a las HREE, las anomalías negativas de Eu y valores medios similares de $(87\text{Sr}/86\text{Sr})_i$, $\epsilon_{\text{Nd}t}$ y $\delta^{18}\text{O}$ para G7 (0.7156 ± 0.0005; - 8.5; 11.49 ‰) y G8 (0.7155 ± 0.0007; - 8.4; 11.39 ‰) muestran que estos dos tipos de granito son el producto de la fusión parcial secuencial del mismo material metasedimentario, del que el granito G8 correspondería a una mayor tasa de fusión parcial que el granito G7.</p> <p>Los granitos G8-G10 y sus minerales muestran una evolución por fraccionación que se puede confirmar mediante la modelización de elementos mayores y traza. Los espectros de REE subparalelos y la disminución de sus contenidos con la diferenciación, la isócrona Rb-Sr para G8, G9 y G10 (315.5 ± 5.4 Ma; MSWD = 1.3) y los valores relativamente uniformes de $\epsilon_{\text{Nd}t}$ y $\delta^{18}\text{O}$ sugieren que la cristalización fraccionada ha sido el principal mecanismo implicado, y habría tenido una duración inferior a 1 Ma.</p> <p>Los granitos especializados estanníferos G7 y G10 tienen contenidos de Sn ≥ 20 ppm, pero los principales filones de cuarzo con casiterita y wolframita cortan al granito G10, que contiene 31 ppm de Sn. La cristalización fraccionada ha sido responsable del aumento del contenido de Sn en los granitos de la serie G8 - G10 y de sus micas.</p>
Corresponding Author:	Rui José dos Santos Teixeira Universidade de Tras-os-Montes e Alto Douro Escola de Ciencias da Vida e do Ambiente Vila Real, Vila Real PORTUGAL
Corresponding Author Secondary Information:	
Corresponding Author's Institution:	Universidade de Tras-os-Montes e Alto Douro Escola de Ciencias da Vida e do Ambiente
Corresponding Author's Secondary Institution:	
First Author:	Rui José dos Santos Teixeira
First Author Secondary Information:	
Order of Authors:	Rui José dos Santos Teixeira Ana Margarida Ribeiro Neiva Maria Elisa Preto Gomes Fernando Corfu Andrés Cuesta Ian W. Croudace
Order of Authors Secondary Information:	
Author Comments:	<p>Dear Editors,</p> <p>I'm submitting the revised manuscript according to the last suggestions of the reviewer, which helped very much to improve the paper "The importance of sequential partial melting and fractional crystallization in the generation of syn-D3 Variscan two-mica granites from the Carrazeda de Ansiães area, northern Portugal". We have implemented all the suggested modifications, which are marked in blue in the annotated version of the revised manuscript. We have also made some other minor corrections in the manuscript, as well as in the Figure 6 and respective caption (marked in blue).</p> <p>We are very grateful for your help,</p>

[Click here to view linked References](#)1 1 **The importance of sequential partial melting and fractional crystallization in the generation of syn-**2 2 **D₃ Variscan two-mica granites from the Carrazeda de Ansiães area, northern Portugal**3 3 R. J. S. Teixeira^{a*}, A. M. R. Neiva[†], M. E. P. Gomes^a, F. Corfu^b, A. Cuesta^c, I. W. Croudace^d4 4 ^a Departament of Geology and Pole of the Geosciences Centre (CGeo), University of Trás-os-Montes e Alto Douro,
5 5 UTAD, Quinta dos Prados, 5000-801, Vila Real, Portugal6 6 ^b Department of Geosciences and Ceed, University of Oslo, PO Box 1047 Blindern, N-0316 Oslo, Norway7 7 ^c Department of Geology, University of Oviedo, C/ Jesús Arias de Velasco s/n, 33005 Oviedo, Spain8 8 ^d Ocean and Earth Science, National Oceanography Centre, Southampton, University of Southampton, European
9 9 Way, Southampton SO14 3ZH, United Kingdom10 10 **Abstract**11 11 At Carrazeda de Ansiães region, northern Portugal, a mesozonal granitic suite intruded Precambrian to Ordovician
12 12 metasedimentary rocks during the late kinematic stages of the Variscan orogeny. In this multiphase granitic complex,
13 13 consisting of ten granite types, the youngest group of two-mica granites (G7 - G10) was emplaced between 318 ± 1
14 14 Ma and 316.2 ± 0.7 Ma, as determined by ID-TIMS U-Pb on zircon and monazite. Granite types G7 - G9 were
15 15 affected by the third phase of deformation (D₃) before they were completely crystallized, as indicated by their internal
16 16 NW-SE magmatic foliation concordant with the regional metasedimentary structures. The granite type G10 shows
17 17 some distinctive textural features, showing a strong brittle deformation, probably due to its preferential emplacement
18 18 in late NNE-SSW fault zones.19 19 Granites G7 - G9 have equal or higher amounts of muscovite than biotite and contain surmicaceous enclaves,
20 20 xenoliths, "schlieren", and, more rarely, microgranular enclaves. The muscovite-dominant granite G10 does not
21 21 contain enclaves. These Variscan granites are peraluminous, with ASI ranging between 1.22 and 1.39 and normative
22 22 corundum of 2.79 – 4.39 %, having the characteristics of S-type granites. In fact, the enrichment in LREE relatively
23 23 to HREE, the negative Eu anomalies, and similar mean values of (⁸⁷Sr/⁸⁶Sr)_i, εNd_t and δ¹⁸O for G7 (0.7156 ± 0.0005;
24 24 – 8.5; 11.49 ‰) and G8 (0.7155 ± 0.0007; – 8.4; 11.39 ‰) show that these two granite types resulted from sequential
25 25 partial melting of the same metasedimentary material, where granite G8 would have derived from a higher degree of
26 26 partial melting than G7.

27 27 * Corresponding author. Tel.: +351 259350364; Fax.: +351 259350480

28 28 E-mail address: rteixeir@utad.pt (R. J. S. Teixeira)

29 29 [†] Deceased in 3rd May 2019.

1 30 Granites G8-G10 and their minerals show a fractionation trend that is confirmed by modeling of major and trace
2 31 elements. The subparallel REE patterns and the decreasing REE contents within the differentiation series, the Rb-Sr
3 32 isochron for G8, G9 and G10 (315.5 ± 5.4 Ma; MSWD = 1.3) and the relatively uniform ϵ_{Nd_t} and $\delta^{18}\text{O}$ data suggest
4 33 that fractional crystallization was the main mechanism, which would have lasted less than 1 Ma. The tin-bearing
5 34 granites G7 and G10 have ≥ 20 ppm Sn, but the main quartz veins containing cassiterite and wolframite cut granite
6 35 G10, which contains 31 ppm Sn. Fractional crystallization was responsible for the increase in Sn content in granites
7 36 from the G8 - G10 series and their micas.
8
9
10
11
12
13
14
15
16
17
18
19
20
21
22
23
24
25
26
27
28
29
30
31
32
33
34
35
36
37
38
39
40
41
42
43
44
45
46
47
48
49
50
51
52
53
54
55
56
57
58
59
60
61
62
63
64
65

Keywords: S-type granites; U-Pb zircon and monazite ages; Isotopic data; Sequential partial melting; Fractional
crystallization; Tin

Resumen

En la región de Carrazeda de Ansiães, norte de Portugal, rocas metasedimentarias de edad Precámbrico y Ordovícico han sido intruídas por una suite granítica mesozonal durante las etapas tardi-cinemáticas de la orogenia Varisca. En esta suite se distinguen diez tipos de granito, de los que los más jóvenes, constituidos por granitos de dos micas (G7 - G10), se emplazan entre 318 ± 1 Ma y 316.2 ± 0.7 Ma, de acuerdo con dataciones U-Pb ID-TIMS en circón y monacita. Los granitos G7 - G9 han sido afectados por la tercera fase de deformación (D_3) antes de su consolidación completa, como sugiere su foliación magmática interna NW-SE concordante con las estructuras metasedimentarias regionales. El granito G10 tiene algunas características texturales distintivas, propias de una fuerte deformación frágil, probablemente debidas a su emplazamiento preferente en zonas de fallas tardías con dirección NNE-SSW. Los granitos G7 - G9 tienen cantidades de moscovita iguales o mayores que las de biotita y contienen enclaves "surmicaceous", xenolitos, "schlieren" y, raras veces, enclaves microgranudos. El granito G10 predominantemente moscovítico no contiene enclaves. Estos granitos variscos son peralumínicos, con valores de ASI entre 1.22 y 1.39, y de corindón normativo entre 2.79 – 4.39%, y presentan características típicas de granitos de tipo S. De hecho, el enriquecimiento en LREE con respecto a las HREE, las anomalías negativas de Eu y valores medios similares de $(^{87}\text{Sr}/^{86}\text{Sr})_t$, ϵ_{Nd_t} y $\delta^{18}\text{O}$ para G7 (0.7156 ± 0.0005 ; - 8.5; 11.49 ‰) y G8 (0.7155 ± 0.0007 ; - 8.4; 11.39 ‰) muestran que estos dos tipos de granito son el producto de la fusión parcial secuencial del mismo material metasedimentario, del que el granito G8 correspondería a una mayor tasa de fusión parcial que el granito G7.

Los granitos G8-G10 y sus minerales muestran una evolución por fraccionación que se puede confirmar mediante la modelización de elementos mayores y traza. Los espectros de REE subparalelos y la disminución de sus contenidos con la diferenciación, la isócrona Rb-Sr para G8, G9 y G10 (315.5 ± 5.4 Ma; MSWD = 1.3) y los valores

1 61 relativamente uniformes de εNd_t y $\delta^{18}\text{O}$ sugieren que la cristalización fraccionada ha sido el principal mecanismo
2 62 implicado, y habría tenido una duración inferior a 1 Ma.
3
4 63 Los granitos especializados estanníferos G7 y G10 tienen contenidos de Sn ≥ 20 ppm, pero los principales filones de
5 64 cuarzo con casiterita y wolframita cortan al granito G10, que contiene 31 ppm de Sn. La cristalización fraccionada ha
6
7 65 sido responsable del aumento del contenido de Sn en los granitos de la serie G8 - G10 y de sus micas.
8
9 66

10 67 **Palabras clave:** Granitos de tipo S; Edades U-Pb en circón y monacita; Datos isotópicos; Fusión parcial secuencial;
11 68 Cristalización fraccionada; Estaño

12 69

13 70

14 71

15 72

16 73

17 74

18 75

19 76

20 77

21 78

22 79

23 80

24 81

25 82

26 83

27 84

28 85

29 86

30 87

31 88

32 89

33 90

34 91

35 92

1 93 **1. Introduction**
2
3 94 Most granitoid plutons in the Central Iberian Zone of the Iberian Massif (Fig. 1a) were formed
4
5 95 and emplaced during the last ductile regional Variscan deformation phase (D_3) (e.g. Ferreira et al., 1987;
6
7 96 Azevedo and Nolan, 1998; Dias et al., 2002; Bea et al., 2003; Valle Aguado et al., 2005; Gutiérrez-
8
9 97 Alonso et al., 2018). At Carrazeda de Ansiães area, northern Portugal, this geological event is well
10
11 98 marked by a suite of ten different S-type granite units, mainly derived by partial melting of
12
13 99 metasedimentary rocks, followed by fractional crystallization or, more rarely, segregated from a
14
15 100 sequential melting process (Teixeira, 2008). This paper reports the geology, mineralogy, petrology,
16
17 101 geochemistry and isotopic compositions (Rb-Sr, Sm-Nd, $\delta^{18}\text{O}$) of the four youngest granite types of the
18
19 102 granitic suite of Carrazeda de Ansiães, belonging to Group II (G7, G8 and G9) and Group III (G10) as
20
21 103 defined by Teixeira (2008). The aim is to understand the processes responsible for their compositional
22
23 104 variability and also the origin of high concentrations of tin in granites G7 and G10 and their micas. In
24
25 105 addition, this study also documents the challenging task of determining the crystallization ages of the four
26
27 106 aforementioned granites by ID-TIMS U-Pb geochronology, in order to verify that they post-date the early
28
29 107 syn- D_3 granites described by Teixeira et al. (2012a) in this area, as it is inferred by the geological field
30
31 108 relations.

33 109
34
35 110 **2. Geological setting**
36

37 111 **2.1. General features**
38

39 112 The Carrazeda de Ansiães area (Northern Portugal) lies in the autochthonous segment of the
40
41 113 Central Iberian Zone of the Iberian Massif that is dominated by a thick sequence of Precambrian to Lower
42
43 114 Paleozoic metasediments deposited onto the ancient margin of Gondwana (Fig. 1; Pereira et al., 2018).
44
45 115 Lower Ordovician volcanic / hypabyssal rocks also occur (e.g. Coke et al., 2011; Teixeira et al., 2013a,
46
47 116 2015). The metasedimentary sequence is known as Dúrico-Beirão Super Group and is subdivided in two
48
49 117 groups: Douro Group and Beiras Group (Oliveira et al., 1992). Large volumes of granitic rocks were
50
51 118 emplaced in the Central Iberian Zone (CIZ) metasediments and ortho-derived rocks **before**, during and
52
53 119 after the third phase of deformation of the Variscan orogeny (D_3), in a period constrained between ca. 347
54
55 120 – 337 Ma and ca. 290 Ma, as indicated by U-Pb data of zircon and monazite (e.g. Valle Aguado et al.,
56
57 121 2005; Martins et al., 2009, 2013; Neiva et al., 2009; Teixeira et al., 2012a; Gutiérrez-Alonso et al., 2018).

1 122 The mesozonal intrusive granitic suite of Carrazeda de Ansiães intruded along the NW-trending
2 123 core of the Vila Real - Torre de Moncorvo antiform formed during the D₁ and D₃ deformation phases
3 124 (Silva et al., 1989; Fig. 1). This is in accordance with the typical spatial distribution of several groups of
4 125 syn-D₃ granites in the Portuguese sector of Central Iberian Zone, occurring along important NW-SE
5 126 alignments that correspond either to the cores of D₃ antiforms or to transcurrent shear zones that would
6 127 have accommodated the horizontal shortening produced in the final stages of the continental collision
7 128 (Ferreira et al., 1987; Dias and Coke, 2006).

15 129 Based on field relationships and petrographic data it is possible to distinguish different types of
16 130 granites in the Carrazeda de Ansiães area (Fig. 1b) that chronologically are arranged as follows: Group I,
17 131 including granite types G1 to G6; Group II, formed by granites G7 to G9; and Group III, constituted only
18 132 by granite G10.

23 133 Group I granites are anisotropic and show evidence of a magmatic foliation that was superposed
24 134 by a more intense subparallel foliation formed in a ductile-brittle regime (Teixeira et al., 2012a). The
25 135 internal structure of these granites (foliation) is concordant to those of the host metasedimentary rocks,
26 136 showing a predominant NW-SE direction. The structural features suggest that granites of Group I would
27 137 already have been consolidated (or at least in a sub-magmatic state) when they were affected by the third
28 138 phase of deformation (D₃) (Teixeira et al., 2011, 2012a).

35 139 Group II granites were apparently deformed by D₃ before being completely crystallized, which
36 140 explains the occurrence of an internal NW-SE magmatic foliation, concordant with the structure of host
37 141 metasediments. This magmatic foliation, more or less penetrative, is given by the orientation of feldspar
38 142 phenocrysts, biotite (Fig. 2a), rarely by muscovite and, in the case of granite G8, by its abundant
39 143 surmicaceous enclaves and xenoliths (Fig. 2b). The dominant magmatic nature of the structure of these
40 144 granites is mainly recognized by the fact that the euhedral feldspar phenocrysts and the quartz crystals of
41 145 the matrix are apparently undeformed (Fig. 2c). On the other hand, granite G10, belonging to Group III,
42 146 shows textural features that suggest a faint overprint by D₃ during its emplacement, intimately associated
43 147 to NNE-SSW fault zones, affected by N60-70° W and N40-50° E secondary joints (Sousa, 2000), and by
44 148 strong brittle deformation (Teixeira, 2008; Fig. 1). However, locally there is evidence of a NW-SE
45 149 magmatic foliation concordant with the regional structure of host metasediments and defined by the
46 150 orientation of feldspar phenocrysts and, sometimes, biotite. Thus, the geometry and localization of the

1 151 different G10 granitic bodies (Fig. 1b) suggest that they were the youngest granite type of the region. The
2 152 magmatic contacts between granites G8 (and G9) and granite G7 are always sharp, and, locally, the latter
3 153 phase can occur in the form of rounded enclaves in granites G8 (Fig. 2d) and G9. There are no visible
4 154 geological contacts between G8, G9 and G10. The geological contacts between granite G10 and G7, and
5 155 to a lesser extent G9, are always defined by NNE-SSW faults (Fig. 1b).

6
7 156 According to the nomenclature of Didier and Barbarin (1991), granites G7, G8 and G9 contain
8 157 surmicaceous enclaves, metasedimentary xenoliths and “schlieren” (Fig. 2b), and rare microgranular
9 158 enclaves. In granite G8 there are irregular to rounded tonalitic enclaves that exhibit sharp contacts with
10 159 the host granite (Fig. 2e), whereas granite G9 contains monzogranite enclaves that should correspond to
11 160 fragments of early cold margins removed during magma ascent (Fig. 2f). The monzogranite enclaves
12 161 partially enclose phenocrysts of the host granite G9 (Fig. 2f). Granite G10 does not contain enclaves.

13 162

14 163 **3. Petrography**

15 164 The most widespread rock type of Group II, G7, as well as G8 and G9, is monzogranite, whereas
16 165 G10 of Group III is alkali feldspar granite since its plagioclase has less than 5% anorthite content (Le
17 166 Maitre et al., 2002). These granites have a subhedral granular texture and contain microcline phenocrysts.
18 167 Plagioclase phenocrysts are only observed in granite G8. They contain quartz, plagioclase, microperthitic
19 168 microcline, biotite, some chlorite, muscovite, zircon, apatite, monazite, ilmenite, rutile and anatase (Table
20 169 1). Granites G7, G9 and G10 also have tourmaline, whereas sillimanite only occurs in granites G7, G8
21 170 and G9. Granite G8 has equal amounts of biotite and muscovite, G7, G9 and G10 are muscovite-dominant
22 171 granites (Table 1).

23 172 Quartz is anhedral and contains inclusions of other minerals (e.g. acicular apatite, rutile, zircon
24 173 and muscovite). In G10, quartz shows undulatory extinction and is intensely fractured (Fig. 2g).

25 174 Microcline is subhedral to anhedral in the matrix, but also forms subhedral microperthitic
26 175 phenocrysts in all granites. It is cross-hatched twinned and contains inclusions of globular quartz,
27 176 plagioclase, biotite, muscovite, zircon and apatite. Plagioclase is subhedral to anhedral and
28 177 polysynthetically twinned. In general, the plagioclase grain boundaries are corroded by microcline,
29 178 muscovite and quartz (Fig. 2g). Their fractures are filled by muscovite and quartz (Fig. 2g). Plagioclase
30 179 phenocrysts only occur in G8 and have a composition of albite-oligoclase. Matrix plagioclase is albite-

1 180 oligoclase in G7, G8 and G9 and albite in G10. Myrmekite occurs locally, while intensely fractured
2 181 feldspars (Fig. 2g) and brecciated aggregates of plagioclase and microcline typically occur in G10.
3
4 182 Biotite and muscovite are commonly subhedral and intergrown, showing textures similar to those
5 183 of primary muscovites of Miller et al. (1981) and Monier et al. (1984). However, some biotite grains are
6
7 184 anhedral and corroded by feldspar and quartz. In the most deformed samples of G10, the micas show
8
9 185 undulatory extinction, deformed cleavage planes and even some fracturing (Fig. 2h). Biotite is strongly
10
11 186 pleochroic from β - and γ - reddish brown to α - yellow. Both micas have inclusions of zircon, monazite,
12
13 187 apatite (Fig. 2i) and ilmenite. Muscovite has rare inclusions of sillimanite.
14
15
16

17 188 Tourmaline is anhedral to subhedral and generally occurs as randomly or concentrically zoned
18 189 crystals. It partially replaces plagioclase and micas, and usually contains inclusions of quartz, micas,
20
21 190 feldspars, zircon and monazite. Tourmaline shows some fracturing, usually filled by quartz.
22
23

24 191 Zircon and monazite are euhedral and occur mainly included in biotite, muscovite and apatite
25 192 (Fig. 2i), and locally in feldspars, quartz and tourmaline. Sillimanite occurs as needles in muscovite of
26
27 193 G7, G8 and G9. Apatite is the most abundant accessory mineral (Fig. 2i), occurring included in micas,
28
29 194 quartz and feldspars. Euhedral to subhedral ilmenite is included mainly in micas, zircon and apatite (Fig.
30
31 195 2i), whereas euhedral rutile is associated to ilmenite and monazite. Secondary muscovite replaces mainly
32
33 196 plagioclase and biotite. Rare, secondary titanite and needle-shaped crystals of rutile are associated to
34
35 197 minor chloritization of biotite.
36
37

38 198
39 **4. Analytical methods**
40

41 200 Samples were crushed in a jaw crusher and grinded in an agate mill. Major and trace elements
42
43 201 were determined by X-ray fluorescence analysis at the National Oceanography Centre, University of
44
45 202 Southampton, UK, using a Philips MagiX Pro PW 2540 wavelength dispersive XRF spectrometer fitted
46
47 203 with a 4 kW Rh target X-ray tube and a VRC Sample Charger (Croudace and Thorpe, 1988; Croudace
48
49 204 and Gilligan, 1990). Relative precision is $\pm 1\%$ for major elements and $\pm 5\%$ for trace elements.
50
51

52 205 The determination of whole rock FeO was carried out by titration with standardised potassium
53
54 206 permanganate solution, whereas H₂O⁺ was determined with a Penfield tube, and Li by atomic absorption
55
56 207 in the Laboratory of Chemistry of the University of Trás-os-Montes e Alto Douro, Vila Real, Portugal.
57
58 208 The precision is $\pm 1\%$ for FeO and H₂O⁺ and $\pm 2\%$ for Li. Fluorine was determined by selective ion
59
60
61
62
63
64

1 209 electrode analysis, with a precision of about 2%, at the SGS Laboratory, Canada (protocol ISE07A).
2 210 The REE[‡] were determined by ICP-MS, with a precision of about 5 %, at the SGS Laboratory,
3 211 Toronto, Canada, following the protocol IMS95R.
4
5 212 Mineral analyses have been determined on an automated wavelength dispersive electron
6 213 microprobe (Cameca Camebax SX-100) at the Scientific-Technical Services of the Department of
7 214 Geology of University of Oviedo, Spain. The analyses were carried out with an accelerating voltage of 15
8 215 kV and a beam current of 15 nA. The precision is better than ± 2 % and the detection limits were
9 216 generally > 0.02 % for most elements.
10
11 217 Trace element analyses of minerals were carried out on a VG Elemental Plasmaquad PQ2+ ICP-
12 218 MS coupled to an ArF Excimer 4D Engineering laser system at the National Oceanography Centre,
13 219 University of Southampton, UK (Gioncada et al., 2005). Measurements were performed using a 20 µm
14 220 laser beam focused on polished 250 µm thick sections. Following a pre-ablation period of 10 s, data were
15 221 collected for 30 s. After collection, the data were corrected for instrumental drift and gas blank, and
16 222 calibrated against the NIST 610 glass standard, where ten repeated measurements were reproducible to ±
17 223 7 %. The detection limits were of 0.1 to 0.5 ppm.
18
19 224 The Sr and Nd isotope analyses were obtained at the Geochronology and Isotope Geochemistry-
20 225 SGIker Facility of the Universidad del País Vasco UPV/EHU (Spain). Samples (0.050 – 0.200 g) were
21 226 digested with HNO₃ + HF in PFA vials (Savillex) and in HF in high pressure PTFE bombs, employing
22 227 the method of Pin and Santos Zaldegui (1997). The isotope ratios were then determined by thermal
23 228 ionization mass spectrometry with a Finnigan MAT 262. Normalization values were ⁸⁶Sr/⁸⁸Sr = 0.1194
24 229 (Steiger and Jäger, 1977) and ¹⁴⁶Nd/¹⁴⁴Nd = 0.7219 (Wasserburg et al., 1981). The values determined for
25 230 the standards are ⁸⁶Sr/⁸⁶Sr = 0.710273 ± 0.000018 (2σ) for NBS 987, and ¹⁴³Nd/¹⁴⁴Nd = 0.511851 ±
26 231 0.000045 (2σ) for La Jolla. The ratios of ⁸⁷Rb/⁸⁶Sr were calculated from the concentrations of Rb and Sr
27 232 determined by wavelength dispersive XRF, whereas the ratios of ¹⁴⁷Sm/¹⁴⁴Nd were calculated from the
28 233 aforementioned ICP-MS data. Precision is ± 1 % for Rb and ± 5 % for Sr, Sm and Nd.
29
30 234 Oxygen isotopic data of whole rock samples were determined by gas mass spectrometry. The gas
31 235 extraction was carried out at the Department of Earth Sciences, University of Western Ontario, Canada,

56 ‡ Main abbreviations used in this article: ICP-MS= Inductively Coupled Plasma Mass Spectrometry;
57 L/M/H REE = Light / Middle / Heavy Rare Earth Elements; ID-TIMS = Isotope Dilution - Thermal
58 Ionization Mass Spectrometry; XRF = X-Ray Fluorescence; MSWD = Mean Sum of Weighted
59 Deviations.

1 236 employing chlorine trifluoride as the reagent (Clayton and Mayeda, 1963). A quartz standard was used
2 237 and the precision was $\pm 0.2 \%$.
3
4 238 Zircon and monazite were concentrated by a combination of magnetic and heavy liquids
5
6 239 separation procedures. Grains were subsequently selected by handpicking under a binocular microscope,
7
8 240 and mechanically air abraded in order to remove external disturbed domains (Davis et al., 1982; Krogh,
9
10 241 1982). The U-Pb isotopic data for those minerals were obtained by ID-TIMS using a Finnigan MAT 262,
11
12 242 at the Department of Geosciences, University of Oslo, Norway, following the standard methodology of
13
14 243 Krogh (1973) with the adaptations described by Corfu and Evins (2002) and Corfu (2004). The decay
15
16 244 constants are those from Jaffey et al. (1971) and the initial Pb correction was done using the compositions
17
18 245 calculated with the Stacey and Kramers (1975) model. The Isoplot program (Ludwig, 1999) was used for
19
20 246 plots and regressions. All uncertainties of analyses are given at the 2σ level. Monazite mounting and their
21
22 247 [backscattered electron \(BSE\)](#) imaging were carried out on the same electron microprobe of University of
23
24 248 Oviedo, Spain.
25
26
27 249
28
29 250 **5. Whole rock geochemistry**
30
31 251 The major and trace element contents of granites G7 to G10 are given in Table 2. The aluminum-
32
33 252 saturation index [$\text{Al} / (2(\text{Ca} - 1.67\text{P}) + \text{Na} + \text{K})$] from 1.22 to 1.39, and normative corundum range from
34
35 253 2.79 to 4.39 %, show that all granites are peraluminous. Plotted in the diagrams of Frost and Frost (2008),
36
37 254 these granites are magnesian and mainly belong to the alkali-calcic series.
38
39
40 255 Selected major and trace elements plotted against total Fe_2O_3 show two distinct regular trends,
41
42 256 mainly defined by curves: a) within the muscovite > biotite granite G7 samples (Fig. 3); b) from the
43
44 257 biotite \approx muscovite granite G8, muscovite > biotite granite G9 to muscovite-dominant granite G10 (Fig.
45
46 258 3a - c and Supplemental electronic Fig. 1). Total Fe_2O_3 has been chosen as differentiation index because it
47
48 259 shows more variability than SiO_2 .
49
50
51 260 The REE contents are low to moderate (64 – 287 ppm) and chondrite-normalized REE patterns
52
53 261 are subparallel within the magmatic series G8 - G9 - G10 (Supplemental electronic data Table 1 and Fig.
54
55 262 4). From G8 to G9 and G10 there is a decrease in the ΣREE and in the enrichment in LREE with respect
56
57 263 to HREE. The negative Eu anomaly also slightly increases from G8 to G9. The REE pattern of G7
58 264 follows a similar trend but it is characterized by a lower La_N/Lu_N average value (21.30) and a higher

1 265 Eu/Eu* value (0.37) than those from granites G8 (40.79 and 0.29, respectively) and G9 (36.21 and 0.27,
2 266 respectively) (Supplemental electronic data Table 1).

3 267 The ocean-ridge granite-normalized diagram (Fig. 5) shows a general negative slope, with Rb,
4 268 Th, Ce (except for G10) and Sm positive anomalies, Ba and Hf negative anomalies, and an enrichment in
5 269 Rb and Th relatively to Nb. These features are characteristic of a crust dominant source (Pearce et al.
6
7 270 1984; Harris et al., 1986). The negative Ba and Hf anomalies suggest fractional crystallization of mainly
8
9 271 K-feldspar and zircon.

10

11 272
12 273 **6. Age and isotopic compositions**

13 274 **6.1. ID-TIMS U-Pb results on zircon and monazite**

14 275 Granites G7 to G10 have a diversified population of zircons, formed by autocrystalline prisms but
15 276 also by short to equant crystals, which commonly contain visible cores. The autocrystalline zircon crystals of
16 277 granites G7 to G10 are generally transparent, colourless to light brown and consist of euhedral prisms
17 278 with terminal pyramid faces. These prisms can reach aspect ratios of up to > 6:1, and commonly have
18 279 melt inclusions. Monazite is euhedral to subhedral.

19 280 In granite G7, the two monazite analyses are reversely discordant (Fig. 6a), which is a common
20 281 feature in this mineral due to the incorporation of significant amounts of ^{230}Th during its crystallization
21 282 that leads to an excess of ^{206}Pb (Schärer, 1984; Corfu and Evans, 2002). Therefore, the weighted average
22 283 $^{207}\text{Pb}/^{235}\text{U}$ age of fractions 6 and 7 of 318 ± 1 Ma is considered the best indication of the crystallization
23 284 age of granite G7. The five analysed zircon fractions from this sample are scattered. Two of them are
24 285 younger than the monazites, probably due to some lead loss (fractions 4 and 5; Table 3 and Fig. 6a). The
25 286 other three deviate towards older ages likely because of inherited components (fractions 1, 2 and 3; Table
26 287 3 and Fig. 6a).

27 288 Zircon fractions 10 and 11 from granite G8 yield a concordia age of 316.2 ± 0.8 Ma (MSWD =
28 289 1.5), whereas the only concordant monazite fraction 12 yields a $^{207}\text{Pb}/^{235}\text{U}$ age of 317.4 ± 0.7 Ma (Table 3
29 290 and Fig. 6b). The combined age of 316.8 ± 1.3 Ma is considered the best indication for the crystallization
30 291 age of this granite. The remaining zircon fractions are discordant, showing lead loss (fraction 9; Fig. 6c)
31 292 and an inherited component (fraction 8; Fig. 6c). A large amount of common lead in the monazite fraction
32 293 13 (25 ppm; Table 3) significantly decreased the precision of the $^{207}\text{Pb}/^{235}\text{U}$ age (309.0 ± 7.9 Ma), which,

1 294 however, still overlaps the combined zircon-monazite age. The monazite fraction 14 is reversely
2 295 discordant yielding an older $^{207}\text{Pb}/^{235}\text{U}$ age of 334.4 ± 1.9 Ma, which could either be caused by uranium
3 296 loss due to an alteration process (Poitrasson et al., 1996; Corfu and Evins, 2002), as evidenced in Fig. 6d,
4 297 or eventually to the presence of an inherited component.
5
6

7 298 Four multi-grain monazite analyses for granite G9 (fractions 19-22) show some dispersion
8 299 (Table 3 and Fig. 6e), which is most probably explained by the presence of inherited components, as
9 300 suggested by the BSE imaging of this mineral (Fig. 6f). Thus, the weighted average of $^{207}\text{Pb}/^{235}\text{U}$ ages of
10 301 the two youngest fractions (20 and 21) is considered the best estimate for the crystallization of granite G9
11 302 (316.6 ± 0.5 Ma). The four analysed zircon fractions are discordant, as they have inherited components.
12
13

14 303 Among the four analysed monazite fractions for granite G10, three are nearly concordant but
15 304 show some dispersion in their $^{207}\text{Pb}/^{235}\text{U}$ ages (Table 3 and Fig. 6g). The BSE imaging also supports the
16 305 existence of inherited components in some monazites of this granite, reason why the $^{207}\text{Pb}/^{235}\text{U}$ age of the
17 306 youngest fraction (29) is considered the most likely age of crystallization of granite G10 (316.2 ± 0.7
18 307 Ma). The remaining monazite fraction (28) is reversely discordant at an older $^{207}\text{Pb}/^{235}\text{U}$ age (341.1 ± 0.8
19 308 Ma). In the granite G10 none of the four zircon fractions is concordant (Fig. 6h), having been affected by
20 309 lead loss (fractions 23 and 24; Table 3 and Fig. 6h) or by the presence of inherited components (fractions
21 310 25 and 26; Table 3 and Fig. 6h).
22
23

34 311 35 36 312 **6.2. Whole rock Rb-Sr, Sm-Nd and oxygen isotope data**

37 313 The Rb, Sr, Sm and Nd isotopic compositions of eleven whole rock samples were analysed
38 314 (Supplemental electronic data Table 2). The initial values calculated for an age of 317 Ma plot within a
39 315 restricted domain from $(^{87}\text{Sr}/^{86}\text{Sr})_i = 0.7133$ for G10 to 0.7161 for G7 and $\epsilon\text{Nd}_t = -9.0$ to -7.6 for G9
40 316 (Fig. 7). Granitic rocks from the Carrazeda de Ansiães area partially match the isotopic composition of
41 317 the Douro Group (Teixeira et al., 2012a) and northern CIZ metasediments (Villaseca et al., 1998, 2008,
42 318 2014), although the hosting metasediments from the Douro Group tend to have somewhat more
43 319 radiogenic Sr and less radiogenic Nd values, ranging from 0.7128 to 0.7188 and from -10.9 to -8.4 ,
44 320 respectively (Fig. 7). Granites G7 to G10 also plot near the isotopic fields established by Villaseca et al.
45
46 321 (1999) for lower crust felsic granulites and orthogneisses from the Spanish Central System. The mean
47
48
49
50
51
52
53
54
55
56
57
58
59
60
61
62
63
64
65

1 322 T_{DM} ages range from 1.28 Ga to 1.86 Ga (Supplemental electronic data Table 2), which are typical values
2 323 for Variscan granites (e.g. Liew and Hofmann, 1988; Dias et al., 2002).

3 324 Three samples of G8, three samples of G9 and two samples of G10 define a Rb-Sr whole rock
4 325 isochron yielding an age of 315.5 ± 5.4 Ma and $(^{87}\text{Sr}/^{86}\text{Sr})_i = 0.7155 \pm 0.0010$ (MSWD = 1.3; Fig. 8).

5 326 This Rb-Sr age overlaps the more precise ages obtained by U-Pb in zircon and monazite.

6
7 327 The mean oxygen isotopic compositions of eight representative samples of granites G7 to G10
8 328 range from 10.93 to 11.49 ‰ (Supplemental electronic data Table 2). Such high $\delta^{18}\text{O}$ values are typical of
9 329 Variscan granitic rocks in Europe (e.g. Hoefs and Emmermann, 1983; Neiva and Gomes, 2001), which
10 330 have been explained by anatexis of metasedimentary sources (Hoefs, 2009).

11 331

12 332 **7. Geochemistry of minerals**

13 333 **7.1. Feldspars**

14 334 The compositions of microcline and plagioclase are given in Supplemental electronic data Table
15 335 3. The orthoclase contents in phenocryst and matrix microcline of granites G7 to G10 are similar (89 to
16 336 98 mol %; Supplemental electronic data Table 3), but the BaO content decreases from phenocryst to
17 337 matrix in all studied granites, suggesting a magmatic origin of this mineral (e.g. Nekvasil, 1992). The
18 338 BaO content in phenocryst microcline is identical in granites G7 and G8 and is higher in the matrix of G8
19 339 than in that of G7. Furthermore, the BaO content of microcline decreases from G8 to G9 and G10
20 340 (Supplemental electronic data Table 3). Some trace elements of matrix microcline plotted versus whole
21 341 rock total Fe_2O_3 define a trend from G8 to G10 (Supplemental electronic data Table 3 and Supplemental
22 342 electronic Fig. 2a). The data for microcline from G7 plot outside this trend (Supplemental electronic Fig.
23 343 2a).

24 344 Plagioclase from granites G7 to G10 is normally zoned, with the anorthite content decreasing
25 345 from core to rim, and from phenocryst to matrix in G8. The anorthite content of matrix plagioclase from
26 346 G8 is higher than that from G7, and decreases from G8 to G9 and G10 (Supplemental electronic data
27 347 Table 3). Some major and trace elements of matrix plagioclase, plotted versus whole rock total Fe_2O_3 ,
28 348 define curvilinear trends from G8 to G9 and G10 (Supplemental electronic data Table 3 and Supplemental
29 349 electronic Fig. 2b). The data for plagioclase from G7 do not fit these trends (Supplemental electronic Fig.
30 350 2b).

1 351 Although the P_2O_5 content of both feldspars is ≤ 0.58 wt.% in granites G7 to G10 (Supplemental
2 352 electronic data Table 3), there is a general increase in P_2O_5 from microcline and plagioclase of G8 to
3 353 those of G9 and G10 (Supplemental electronic data Table 3). The microcline contains more P_2O_5 than
4 354 coexisting plagioclase, which is in accordance with findings by London et al. (1990), Neiva (1998) and
5 355 Antunes et al. (2008). The empirical distribution coefficient $D[P]Kf/Pl$ between K-feldspar and
6 356 plagioclase ranges from 1.38 and 3.00. This coefficient should be about 1.2 in natural feldspars, close to
7 357 their orthoclase and albite end members, when in equilibrium (London et al., 1999). Granite G10 has
8 358 $D[P]Kf/Pl = 3.00$ indicating that its microcline started to crystallize before albite or, eventually, that albite
9 359 was formed from a magma already depleted in phosphorous.

10 360
11
12 361 **7.2. Micas**

13 362 The average compositions of biotite and muscovite are given in Supplemental electronic data
14 363 Table 4. Biotites have $Mg/(Mg + Fe^{2+} + Fe^{3+})$ ranging from 0.16 – 0.36 (Rieder et al., 1999) and
15 364 compositions similar to those found in biotites from aluminium-potassic rock series of the biotite ±
16 365 cordierite and biotite ± muscovite fields (Nachit et al., 1985). The biotites from G8 - G10 define
17 366 fractionation trends for major and trace elements. In general, the data for biotite from G7 do not fit those
18 367 trends (Supplemental electronic Fig. 3a).

19 368 Muscovites from G7 to G10 have high TiO_2 and Al_2O_3 and low MgO contents (Supplemental
20 369 electronic data Table 4) and so are magmatic (Miller et al., 1981; Monier et al., 1984). Variation diagrams
21 370 for major and trace elements of muscovite versus whole rock total Fe_2O_3 show a trend from G8 to G10
22 371 but do not include G7 (Supplemental electronic Fig. 3b).

23 372
24
25 373 **7.3. Ilmenite**

26 374 Ilmenite occurs in all granites and its mean Mn content ranges from 0.137 and 0.274 pfu
27 375 (Supplemental electronic data Table 5). Negative correlations were found between Mn and Fe^{2+} , and
28 376 between Ti and $Fe^{2+} + Fe^{3+} + Mn$ of ilmenite from granites G7 to G10. Mn and $Mn/(Mn + Fe^{2+})$ increase
29 377 and Fe^{2+} decreases from the ilmenite of G8 to the ilmenite of G9 and G10 (Supplemental electronic Fig.
30 378 3c).

31 379

380 8. Regional correlation

The majority of granitic rocks from the Central Iberian Zone were emplaced at upper and middle crustal levels during the deformation phase (D_3), following the crustal thickening and subsequent extension related to the Variscan continent-continent collision (Gutiérrez-Alonso et al., 2018). Therefore, the granitic rocks from northern and central Portugal have been classified according to their relation with the aforementioned deformation phase as: syn-orogenic pre- D_3 , syn- D_3 ($\sim 320 - 310$ Ma) and late- D_3 ($310 - 300$ Ma), and late- to post orogenic (post- D_3) ($\sim 296 - 290$ Ma) (Dias et al., 1998; Ferreira et al., 1987; Valle Aguado et al., 2005). The U-Pb geochronological data for the studied granites, together with the geological field relations, may be interpreted as reflecting two generations of syn- D_3 granites: 1) the oldest is granite G7 formed at 318 ± 1 Ma; 2) the youngest, formed in the interval of 316.8 ± 1.3 Ma and 316.2 ± 0.7 Ma, includes granites G8 to G10. The compositions of these granites project in the field of syn-collision granites in the R_1 - R_2 diagram (La Roche et al., 1980; Batchelor and Bowden, 1985) and also in the tectonic discrimination diagrams of Pearce et al. (1984).

393

9. Petrogenesis

9.1. Anatectic granitic rocks and their protoliths

Major and trace elements variations suggest that the muscovite > biotite granite G7 and the biotite ≈ muscovite granite G8 formed during distinct magmatic pulses (Fig. 3a - c). Evidence includes the REE patterns, with a distinct enrichment in the LREE (Fig. 4), trace and major elements in microcline (Supplemental electronic Fig. 2a), plagioclase (Supplemental electronic Fig. 2b), biotite (Supplemental electronic Fig. 3a) and muscovite (Supplemental electronic Fig. 3b), but also the existence of intrusive and sharp contacts between granites G8 (and G9) and the granite G7, whereas those between granite G10 and G7 and, to a lesser extent, G9, are always associated to NNE-SSW faults. There are no visible intrusive contacts between G8, G9 and G10 (Fig. 1).

Granites G7 and G8 are peraluminous, with ASI ranging from 1.22 to 1.39 (Table 1), and hence contain aluminum-rich minerals such as biotite, muscovite and sillimanite. These granites also have ilmenite, $K_2O > Na_2O$, low CaO/Na_2O , an enrichment in LREE relative to HREE, negative Eu anomalies, $(^{87}Sr/^{86}Sr)_i = 0.7136$ to 0.7160 , $\epsilon Nd_t = -9.0$ to -7.6 and $\delta^{18}O = 10.93$ to 11.49‰ (Supplemental electronic data Table 2), highlighting their affinity to S-type magmas (Chappell and White, 1992). Taking

1 409 into account that metapelitic rocks have $\text{CaO}/\text{Na}_2\text{O} < 0.5$, in contrast to metagreywacke or meta-igneous
2 410 rocks with $\text{CaO}/\text{Na}_2\text{O} = 0.3 - 1.5$, Jung and Pfänder (2007) used this ratio to infer the source composition
3 411 of peraluminous granites. In granites G7 and G8 the $\text{CaO}/\text{Na}_2\text{O}$ ratios are 0.18 and 0.27, respectively,
4 412 which supports an origin from a mainly metapelitic source. Furthermore, the similarity in the mean
5 413 ($^{87}\text{Sr}/^{86}\text{Sr}$)_i and $\varepsilon_{\text{Nd},t}$ values of granites G7 and G8 also indicate that these magmas were formed by partial
6 414 melting of a common metapelitic source with a composition comparable to those of Douro Group and
7 415 northern CIZ metasediments (Villaseca et al., 1998, 2008, 2014; Teixeira et al., 2012a). The U-Pb ID-
8 416 TIMS data allow to infer that granites G7 and G8 contain Neoproterozoic inherited zircon components
9 417 (cores, most likely) with ages comparable to those of detrital zircons in metasediments of the Douro
10 418 Group (e.g. Teixeira et al., 2012b, 2013b), thus supporting their involvement in the origin of the granitic
11 419 magmas. A fairly identical model involving the partial melting of Neoproterozoic to lower Palaeozoic
12 420 supracrustal rocks has also been proposed to explain the origin the Variscan granites in the Eastern
13 421 Erzgebirge / Krušné hory, Central Europe (e.g. Förster and Romer, 2010; Romer et al., 2011; Breiter,
14 422 2012). However, it should be reminded that the isotopic composition of granitic magmas derived from a
15 423 source at depth does not necessarily have a one-to-one relationship, particularly concerning Sr, to the
16 424 equivalent metamorphic rocks at the level of granitic emplacement. In fact, Miller et al. (1992) and
17 425 Villaseca et al. (1999) argue that, in orogenic areas, granite sources are not the outcropping metamorphic
18 426 rocks, but those located at deeper crustal levels.

37 427 Although the geochemical and isotopic signatures of granites G7 and G8 indicate a major role of
38 428 a supracrustal protolith in the genesis of these magmas, the granite G8 of Carrazeda de Ansiães area also
39 429 contains some tonalitic enclaves, which may point to a local interaction between felsic crustal melts and
40 430 mafic to intermediate mantle-derived magmas, enough to generate somewhat more primitive isotopic
41 431 signatures, as for instance in sample GQV9 of granite G8. This mechanism has also been invoked to
42 432 explain the origin of Variscan granitic intrusions elsewhere in the Central Iberian Zone (e.g. Costa et al.,
43 433 2014; Gomes et al., 2014) and in the French Massif Central (e.g. Williamson et al., 1996; Ledru et al.,
44 434 2001), as well as to explain the whole range of compositions and geochemical trends of granites of the
45 435 Peninsula pluton, South Africa (Garcia-Arias and Stevens, 2017).

55 436
56 437 *9.2. Sequential partial melting of G7 and G8*

1 438 Granite G7 has a lower biotite / muscovite proportion (0.5) than G8 (1.0). From G7 to G8 there
2 439 is an increase in Zr, Th, TiO₂, MgO, CaO, V, Ni, Sr and Ba with increasing Fe₂O₃_t (Fig. 3b - j), indicating
3 440 that granite G8 could result from a higher degree of partial melting than granite G7 (Holtz [and](#) Barbey,
4 441 1991). Furthermore, granite G7 shows geochemical trends in the variation diagrams (Fig. 3) that seem to
5 442 continue into G8, suggesting a relation between both granites. However, a fractional crystallization
6 443 process is not adequate to explain their genesis because G7 is the most evolved and [was](#) emplaced up to ~
7 444 1 Ma earlier than granite G8. These two granites have identical Rb, (⁸⁷Sr/⁸⁶Sr)_i, εNd_t and δ¹⁸O values and
8 445 subparallel REE patterns, but granite G8 is richer in ΣREE and has higher La_N/Lu_N average values than
9 446 G7 (Fig. 4). Both granites also contain surmicaceous enclaves but these are much more abundant in
10 447 granite G8, which is compatible with a higher degree of partial melting (Holtz [and](#) Barbey, 1991;
11 448 Teixeira, 2008).

12 449 An estimate of the temperature of formation of unfractionated granitic magmas can be obtained
13 450 from the Al₂O₃/TiO₂ ratio, since magmas with low ratios are generated at higher temperatures than those
14 451 with high Al₂O₃/TiO₂ ratios (Sylvester, 1998; Jung and Pfänder, 2007). On this basis, granite G8
15 452 (Al₂O₃/TiO₂ = 34.74) originated at a higher temperature than G7 (Al₂O₃/TiO₂ = 72.53). The conditions of
16 453 formation of granitic magmas can also be obtained from the zircon saturation equation (Watson and
17 454 Harrison, 1983), assuming equilibrium conditions. The average zircon saturation temperature (T_{zr}) is of
18 455 816 °C for G8 and 734 °C for G7, which indicates a higher degree of partial melting for G8 (Miller et al.,
19 456 2003). However, these T_{zr} values are overestimated since there are inherited zircon cores in both granites
20 457 (Watson and Harrison, 1983).

21 458 Matrix microcline from G8 has a higher Ba content than the corresponding microcline in G7
22 459 (Supplemental electronic data Table 3), while anorthite content of matrix plagioclase from G8 is higher
23 460 than that from G7 (Supplemental electronic data Table 3). Both phenocryst- and matrix- feldspars from
24 461 G8 have less P₂O₅ than those in G7 (Supplemental electronic data Table 3). Biotite and muscovite from
25 462 G8 have more MgO and less Li than those from G7 (Supplemental electronic data Table 4), whereas
26 463 muscovite from G7 is richer in F than that from G8 (Supplemental electronic data Table 4). Therefore, the
27 464 mineral compositions support that G8 was formed at a higher temperature than G7 and also confirm that
28 465 they are not related by a fractional crystallization mechanism.

1 466 The apparently sequential partial melting evolution from **muscovite > biotite** granite G7 (318 ± 1
2 467 Ma) to biotite ~ muscovite granite G8 (316.8 ± 1.3 Ma) from Carrazeda de Ansiães area is comparable to
3 468 that observed for other Portuguese Variscan granites, namely those from the Tourém area (Holtz and
4 469 Barbey, 1991; Neiva, 1994), the Guarda-Sabugal area (Neiva et al., 2011a) and the Penafiel area
5 470 (Carvalho et al., 2012), and also in other areas elsewhere, e.g. those in the Achiras complex, Córdoba,
6 471 Argentina (Otamendi et al., 1998).

7 472 The generation of granitic rocks from the same source by sequential partial melting is a rare
8 473 process, whose occurrence in Portugal is mainly explained by the combination of an intense crustal
9 474 thickening during the Variscan orogeny that **established** a high geothermal gradient, and the subsequent
10 475 collapse, extension and mantle upwelling (Clemens, 2003; Valle Aguado et al., 2005; Gutiérrez-Alonso et
11 476 al., 2018). At Carrazeda de Ansiães area, this is also supported by the presence of scarce tonalitic
12 477 enclaves in granite G8, formed at higher temperatures, and their absence in granite G7.

13 478

14 479 **9.3. Series of fractional crystallization**

15 480 Granites G8, G9 and G10, with identical crystallization ages, at 316.8 ± 1.3 Ma, 316.6 ± 0.5 Ma
16 481 and 316.2 ± 0.7 Ma, respectively, but with no visible intrusive contacts, seem to define a magmatic
17 482 differentiation series as they define curvilinear trends in major and trace elements diagrams (Fig. 3a - c
18 483 and Supplemental electronic Fig. 1), and show decreasing Ba contents of phenocryst and matrix
19 484 microcline (Supplemental electronic data Table 3), decreasing anorthite content of plagioclase
20 485 (Supplemental electronic data Table 3), fractionation trends for microcline (Supplemental electronic Fig.
21 486 2a), plagioclase (Supplemental electronic Fig. 2b), biotite (Supplemental electronic Fig. 3a), muscovite
22 487 (Supplemental electronic Fig. 3b) and ilmenite (Supplemental electronic Fig. 3c), and subparallel whole
23 488 rock REE patterns within each series (Fig. 4). The decrease in LREE from G8, to G9 and G10 can be
24 489 explained by fractionation of monazite (Bea, 1996), whereas the decrease in the MREE can be due to
25 490 apatite fractionation (Henderson, 1984), and the decrease in HREE to zircon fractionation (Yurimoto et
26 491 al., 1990; Bea, 1996), in agreement with the decrease in Zr from G8 to G9 and G10 (Table 2). The Sr and
27 492 Nd isotopic compositions are relatively uniform, although with some differences in G8, G9 and G10 and
28 493 even within each granite type (Fig. 7). There is no significant variation in $\delta^{18}\text{O}$ values, which also
29 494 supports a fractional crystallization mechanism. The slightly decrease in the $\delta^{18}\text{O}$ value of granite G10

1 495 can be attributed to some oxygen-isotope exchange at subsolidus temperature between feldspar and quartz
2 496 (Blattner et al., 2002). Furthermore, ($^{87}\text{Sr}/^{86}\text{Sr}$)_I versus 1/Sr does not define a positive correlation for the
3 497 series, which would confirm that assimilation or mixing processes did not play a major role.
4
5
6

7 498 Major and trace element contents were used for testing fractional crystallization. The average of
8 499 the two least silicic samples of granite G8 was selected as the starting magma, while the average of the
9 500 two most silicic samples of G8, the average of samples GC8 and GC7 of granite G9 and three samples of
10 501 G10 (GAJ13, GAJ8 and GAJ11), free of metasomatic effects, were selected as residual liquids. The least-
11 502 squares regression method was applied to model major elements using pure anorthite, albite, K-feldspar
12 503 and quartz compositions together with the compositions of biotite and ilmenite analysed with the electron
13 504 microprobe in the G8 sample with the lowest SiO₂ content. The calculated compositions of parent magma
14 505 for the granites compare well with the respective determined parent granite and the sum of the squares of
15 506 the residuals ΣR^2 is ≤ 0.0115 (Supplemental electronic data Table 6). The anorthite content of
16 507 fractionating plagioclase in the cumulate is close to that of the core of plagioclase phenocrysts in the G8
17 508 sample with the lowest SiO₂. The percentages of quartz and K-feldspar increase and those of plagioclase,
18 509 biotite and ilmenite decrease in the cumulate versus the decrease in the weight fraction of melt remaining
19 510 during fractional crystallization (Supplemental electronic data Table 6). The perfect (or Rayleigh)
20 511 fractional crystallization equation, the modal compositions of cumulate and weight fraction of melt
21 512 remaining during fractional crystallization, based on calculations involving major elements and the
22 513 distribution coefficients of Arth (1976) and Nash and Crecraft (1985), were used for modelling Sr, Ba and
23 514 Rb, which are the most informative trace elements for evaluating the fractionation of granitic rocks.
24
25 515 Strontium and Ba decrease and Rb increases with the decrease in the remaining melt during fractional
26 516 crystallization from G8 to G9 and G10 (Supplemental electronic data Table 6). The calculated Sr, Ba and
27 517 Rb values are consistent with the measured data although the calculated Sr and Ba values for G10 are
28 518 generally higher and the calculated Rb, Rb/Ba and Rb/Sr ratios are lower than the measured data
29
30 519 (Supplemental electronic data Table 6 and Supplemental electronic Fig. 4). This may be due to
31
32 520 uncertainties in the distribution coefficients and the possibility that magmatic fluids might have controlled
33
34 521 the behaviour of LIL elements in the most evolved granitic rocks (e.g. Neiva 1998; Antunes et al., 2008;
35
36 522 Huang et al., 2014; Xu et al., 2015; Romer and Kroner, 2016; Pan et al., 2018; Roda-Robles et al., 2018;
37
38 523 Nguyen et al., 2019).

1 524 The described process is in agreement with the studies done on other European Variscan granitic
2 525 plutons where fractional crystallization contributed to an enrichment in lithophile and fluxing elements,
3 526 namely in granites of the Cornubian batholith, England (Müller et al., 2006; Simons et al., 2016, 2017;
4 527 Smith et al., 2019), in some granites of Krušné hory / Erzgebirge Mountains, Central Europe (Breiter,
5 528 2012), in the highly evolved peraluminous granite of Belvís de Monroy, Spain (Merino Martínez et al.,
6 529 2014), but also in granitic suites elsewhere, e.g. along the southeastern margin of the North China Craton
7 530 (Li et al., 2020), in the Mufushan complex, South China (Wang et al., 2014) and in the Lhasa Terrane,
8 531 southern Tibet (Zhang et al., 2019).

17 532

18

19 **533 10. Tin content of granites and its origin**

20

21 534 Among the late syn-D₃ granitic suite of Carrazeda de Ansiães (G7 - G10), the only Sn-bearing
22 535 granites in the sense of Neiva (1984) and Lehmann (1990) are the muscovite > biotite granite G7 and
23 536 muscovite-dominant granite G10, with mean Sn contents of 20 and 31 ppm, respectively (Table 2). The
24 537 main occurrences of tin- and tungsten-bearing quartz veins are in granite G10, but some are also spatially
25 538 related with G7.

26

27

28

29

30

31 539 The role of fractional crystallization in the genesis of tin-mineralized early syn-D₃ granites (G1 -
32 540 G6) from Carrazeda de Ansiães area has been previously evidenced by Teixeira et al. (2012a).
33 541 Nevertheless, this mechanism is recurrently invoked to explain the occurrence of Sn-bearing granites in
34 542 similar geological contexts (Neiva, 1984, 2002; Lehmann, 1990; Gomes and Neiva, 2002; Neiva et al.,
35 543 2011b; Jiang et al., 2015; Ding et al., 2017; Chen et al., 2018; Feng et al., 2018). The absence of
36 544 cassiterite in the independent magmatic pulse G7 and in granites of the differentiation series G8 - G10
37 545 precludes a significant retention of Sn in micas. There is indeed a progressive enrichment in Sn from G8
38 546 to G9 and G10, which may be explained by its increase in the hosted biotite and primary muscovite (Fig.
39 547 9). This points to a concentration conditioned by a fractional crystallization mechanism, where the low
40 548 fO₂ favours the enrichment of Sn in residual liquids (Lehmann, 1990; Chicharro et al., 2016; Qiu et al.,
41 549 2017; Roda-Robles et al., 2018; Cao et al., 2020; Cruz et al., 2020). In the log Sn – log Rb/Sr plot (Fig.
42 550 10) the correlation line for G8, G9 and G10 follows a Sn enrichment where the fractionation trend is
43 551 traceable back to below 1 ppm Sn in the least evolved portions, showing that there was no primary Sn

1 552 enrichment (Lehmann, 1990), in agreement with the low Sn values of the host metasedimentary rocks (<
2 553 5 ppm; Teixeira et al., 2012a). Therefore these granites do not reflect a crustal anomaly in Sn.
3
4

5 554 Despite the similar to marginally lower Sn contents in primary muscovite, when compared to
6 555 those in the coexisting biotite (Supplemental electronic data Table 4 and Fig. 9), muscovite would retain
7 556 more Sn than biotite due to its higher abundance in the rock (Table 2). In fact, of the total amount of Sn in
8
9 557 the whole rock, primary muscovite would retain an average of 15 % in G7, 15 % in G8, 15 % in G9 and
10 558 18 % in G10, while biotite would hold an average of 14 % in G7, 15 % in G8, 10 % in G9 and 4 % in
11
12 559 G10. Therefore, with the increasing degree of differentiation from G7 to G10, the percentage of Sn
13
14 560 retained in muscovite tends to increase, while that retained in biotite decreases.
15
16

17 561 The tin-bearing granites from the Central Iberian Zone are the parent rocks of mineralisations
18 562 that mainly occur in pegmatites and quartz veins (Neiva, 1984; Lehmann, 1990; Almeida et al., 2002;
19
20 563 Neiva and Ramos, 2010), although cassiterite may also occur in some aplites (Charoy and Noronha,
21
22 564 1996), greisens (Wang et al., 2017) and locally in granites (Gomes and Neiva, 2002). In general, these
23
24 565 specialized granites result from the partial melting of metasedimentary rocks, as indicated by Sr and Nd
25
26 566 isotope data from different areas of Portugal and Spain (Neiva, 2002; Neiva et al., 2009, 2011a; Ruiz et
27
28 567 al., 2008), other domains of the Variscan orogenic belt, like the Cornubian batholith, England (Müller et
29
30 568 al., 2006) and Erzgebirge, Germany (Romer et al., 2016), and elsewhere, e.g. in the W-Sn polymetallic
31
32 569 metallogenic belt at the southeast Yunnan Province in the southwestern Yangtze Block, South China (Liu
33
34 570 et al., 2020).

35
36 571
37
38 572 **11. Conclusions**

39
40
41 573 This study in northern Portugal concerns a mesozonal granitic suite intruded into Precambrian to
42
43 574 Ordovician metasedimentary rocks during the syn-kinematic stages of the Variscan orogeny. This
44
45 575 multiphase granitic complex evolved as ten intrusive phases as identified from field, geochemical and
46
47 576 isotopic data.

48
49
50 577 Granites of Group II (G7 - G9) display an internal NW-SE foliation concordant with the regional
51
52 578 metasedimentary structures, suggesting that they were affected by the last stages of the third phase of
53
54 579 deformation (D_3) of the Variscan orogeny while in the magmatic state. Granite G10 belongs to Group III
55
56 580 and is characterized by a strong brittle deformation, probably due to its preferential emplacement in late
57
58
59
60
61
62
63
64

1 581 NNE-SSW fault zones. The U-Pb ages for zircon and monazite show that these granites are the youngest
2 582 of the Carraceda de Ansiães area (318 ± 1 Ma to 316.2 ± 0.7 Ma).

3 583 Granites G7 and G8 are peraluminous and have similar $(^{87}\text{Sr}/^{86}\text{Sr})_{\text{317}}$, $\varepsilon\text{Nd}_{\text{317}}$ and $\delta^{18}\text{O}$ values, but
4 584 distinct major, trace and rare earth element contents and compositions of feldspars and micas. Granite G8
5 585 resulted from a higher degree of partial melting of the same metasedimentary source, probably
6 586 metapelitic, than granite G7.

7 587 Granite G8 magma evolved by fractional crystallization, which is confirmed by the major and
8 588 trace element trends defined by G8, G9 and G10, the decrease in REE contents from G8 to G10, their
9 589 similar $(^{87}\text{Sr}/^{86}\text{Sr})_{\text{i}}$, $\varepsilon\text{Nd}_{\text{i}}$ and $\delta^{18}\text{O}$ values, but also by the compositions of feldspars and micas. Granites
10 590 G9 and G10 are derived from granite G8 magma by fractionation of quartz, K-feldspar, plagioclase,
11 591 biotite and ilmenite.

12 592 Fractional crystallization increased the Sn content of magma within the G8-G9-G10 series. Tin-
13 593 bearing granites G7 and G10 do not represent a crustal anomaly of Sn.

14 594 The high geothermal gradients due to the middle Carboniferous Variscan continent-continent
15 595 collision and the subsequent post-thickening extension, probably accompanied by the intrusion of mantle-
16 596 derived magmas in the lower crust, caused partial melting of crustal material.

17 597
18 598 **12. Acknowledgements**

19 599 This paper corresponds to a part of the PhD thesis of R. J. S. Teixeira. We are grateful to Prof.
20 600 Robert Nesbitt who managed the EU SOCFAC facility (HPRI-1999-CT-00108) that led to access to
21 601 geochemical facilities at the University of Southampton (United Kingdom), Dr. Andy Milton (at the same
22 602 institution) for the skilled assistance in the laser ablation ICP-MS laboratory, Prof. José Ignacio Gil
23 603 Ibarguchi, Dr. Sonia García de Madinabeitia and Dr. María Eugenia Sanchez Lorda for the Rb-Sr and
24 604 Sm-Nd isotopic data obtained at the Geochronology and Isotope Geochemistry- SGIker Facility of the
25 605 Universidad del País Vasco UPV/EHU (Spain). Prof. Fred J. Longstaffe for the oxygen-isotope
26 606 analyses obtained at the Department of Earth Sciences, University of Western Ontario (Canada). R. J. S.
27 607 Teixeira also thanks to Álvaro Miranda, Dr. Alvaro Rubio, Márcio Silva, Miguel Fernández, Nelson
28 608 Pinto, Simão Botelho and Tito Azevedo for their help in field and laboratory works. Funding was
29 609 provided to R. J. S. Teixeira by the SFRH/BD/17246/2004 PhD grant from FCT - Fundação para a

1 610 Ciéncia e a Tecnologia, Portugal, and another grant from SOCFAC (Southampton Oceanography Centre,
2
3 611 Facilities and Co-Operation). This research was financially supported by the Pole of the Geosciences
4
5 612 Centre (CGeo) and projects UIDB/00073/2020 and UIDP/00073/2020 through FCT - Portuguese
6
7 613 Foundation for Sciences and Technology. Very helpful constructive reviews and comments were
8
9 614 provided by two anonymous referees. We are also grateful to the Guest Editors for the final comments.
10
11 615
12
13 616
14
15 617
16
17 618
18
19 619
20
21 620
22
23 621
24
25 622
26
27 623
28
29 624
30
31 625
32
33 626
34
35 627
36
37 628
38
39 629
40
41 630
42
43 631
44
45 632
46
47 633
48
49 634
50
51 635
52
53 636
54
55 637
56
57 638
58
59
60
61
62
63
64
65

- 1 639 **References**
- 2 640 Almeida, M. A., Martins, H. C. & Noronha, F. (2002). Hercynian acid magmatism and related
- 3 641 mineralizations in Northern Portugal. *Gondwana Research*, 5, 423–434.
- 4
- 5 642 Antunes, I. M. H. R., Neiva, A. M. R., Silva, M. M. V. G., & Corfu, F. (2008). Geochemistry of S-type
- 6 643 granitic rocks from the reversely zoned Castelo Branco pluton (central Portugal). *Lithos*, 103(3–4),
- 7 644 445–465. <https://doi.org/10.1016/j.lithos.2007.10.003>
- 8
- 9 645 Arth, J. G. (1976). Behaviour of trace elements during magmatic processes – a summary of theoretical
- 10
- 11 646 models and their applications. *Journal of Research of the United States Geological Survey*, 4, 41–47.
- 12
- 13 647 Azevedo, M. R. & Nolan, J. (1998). Hercynian late-post-tectonic granitic rocks from the Fornos de
- 14
- 15 648 Algodes area (Northern Central Portugal). *Lithos*, 44(1–2), 1–20. [https://doi.org/10.1016/S0024-4937\(98\)00019-X](https://doi.org/10.1016/S0024-4937(98)00019-X)
- 16
- 17 649 Azevedo, M. R. & Valle Aguado, B. (2006). Origem e instalação de granitóides variscos na Zona Centro-
- 18
- 19 650 Ibérica. In Dias, R., Araújo, A., Terrinha, P., Kullberg, J. (Eds.), *Geologia de Portugal no contexto da*
- 20
- 21 651 *Ibérica* (pp. 107–121). Évora: Universidade de Évora.
- 22
- 23 652 Batchelor, R. A. & Bowden P. (1985). Petrogenetic interpretation of granitoid rock series using
- 24
- 25 653 multicationic parameters. *Chemical Geology*, 48, 43–55.
- 26
- 27 654 Bea, F. (1996). Residence of REE, Y, Th and U in granites and crustal protoliths; implications for the
- 28
- 29 655 chemistry of crustal melts. *Journal of Petrology*, 37(3), 521–552.
- 30
- 31 656 <https://doi.org/10.1093/petrology/37.3.521>
- 32
- 33 657 Bea, F., Montero, P. & Zinger, T. (2003). The Nature and Origin of the Granite Source Layer of Central
- 34
- 35 658 Iberia: Evidence from Trace Element, Sr and Nd Isotopes, and Zircon Age Patterns. *Journal of*
- 36
- 37 659 *Geology*, 111, 579–595.
- 38
- 39 660 Beetsma, J. J. (1995). *The late Proterozoic/Paleozoic and Hercynian crustal evolution of the Iberian*
- 40
- 41 661 *Massif, N Portugal*. Unpublished PhD thesis, Vrije Universiteit Amsterdam, 223 p.
- 42
- 43 662 Blattner, P., Abart, R., Adams, C. J., Faure, K. & Hui, L. (2002). Oxygen isotope trends and anomalies in
- 44
- 45 663 granitoids of the Tibetan plateau. *Journal of Asian Earth Sciences*, 21(3), 241–250.
- 46
- 47 664 Breiter, K. (2012). Nearly contemporaneous evolution of the A- and S-type fractionated granites in the
- 48
- 49 665 Krušné hory/Erzgebirge Mts., Central Europe. *Lithos*, 151, 105–121.
- 50
- 51 666 <https://doi.org/https://doi.org/10.1016/j.lithos.2011.09.022>
- 52
- 53
- 54
- 55
- 56
- 57
- 58
- 59
- 60
- 61
- 62
- 63
- 64
- 65

- 1 668 Bruyin, H., Westhuizen, W. A. & Schoch, A. E. (1983). The estimation of FeO, F, and H₂O⁺ by
2 669 regression in microprobe analysis of natural biotite. *Journal of Trace and Microprobe Techniques*, 1,
3 670 399–413.
- 4 671 Cao, J., Wu, Q., Yang, X., Deng, X., Li, H., Kong, H., & Xi, X. (2020). Geochemical factors revealing
5 672 the differences between the Xitian and Dengfuxian composite plutons, middle Qin-Hang Belt:
6 673 Implications to the W–Sn mineralization. *Ore Geology Reviews*, 118.
7 674 <https://doi.org/10.1016/j.oregeorev.2020.103353>
- 8 675 Carvalho, P. C. S., Neiva, A. M. R., Silva, M. M. V. G., & Corfu, F. (2012). A unique sequential melting
9 676 mechanism for the generation of anatetic granitic rocks from the Penafiel area, northern Portugal.
10 677 *Lithos*, 155, 110–124. <https://doi.org/10.1016/j.lithos.2012.08.019>
- 11 678 Chappell, B. W., White, A. J. R. (1992). I- and S-type granites in the Lachlan Fold Belt. *Transactions of*
12 679 *the Royal Society of Edinburgh Earth Sciences*, 83, 1–26.
- 13 680 Charoy, B., Noronha, F., 1996. Multistage growth of a rare-element volatile-rich microgranite at
14 681 Argemela (Portugal), *Journal of Petrology*, 37, 73–94.
- 15 682 Chen, X., Liang, H., Richards, J. P., Huang, W., Zhang, J., Wu, J., & Sotiriou, P. (2018). Age and granite
16 683 association of skarn W mineralization at Niutangjie district, South China Block. *Ore Geology*
17 684 *Reviews*, 102, 268–283. <https://doi.org/10.1016/j.oregeorev.2018.09.003>
- 18 685 Chicharro, E., Boiron, M. C., López-García, J. Á., Barfod, D. N., & Villaseca, C. (2016). Origin, ore
19 686 forming fluid evolution and timing of the Logrosán Sn-(W) ore deposits (Central Iberian Zone,
20 687 Spain). *Ore Geology Reviews*, 72, 896–913. <https://doi.org/10.1016/j.oregeorev.2015.09.020>
- 21 688 Clayton, R. N. & Mayeda, T. K. (1963). The use of bromine pentafluoride in the extraction of oxygen
22 689 from oxides and silicates for isotopic analysis. *Geochimica et Cosmochimica Acta*, 27, 43–52.
- 23 690 Clemens, J. D. (2003). S-type granitic magmas – petrogenetic issues, models and evidence. *Earth-Science*
24 691 *Reviews*, 61, 1–18.
- 25 692 Coke, C. J. M., Teixeira, R. J. S., Gomes, M. E. P., Corfu, F. & Rubio Ordóñez, A. (2011). Early
26 693 Ordovician volcanism in Eucísia and Mateus areas, Central Iberian Zone, northern Portugal
27 694 (Goldschmidt Conference Abstract). *Mineralogical Magazine*, 75(3), 685.
- 28 695 Corfu, F. & Evans, P. M. (2002). Late Paleoproterozoic monazite and titanite U–Pb ages in the Archean
29 696 [Suomujärvi](#) complex, N Finland. *Precambrian Research*, 116, 171–181.

- 1 697 Corfu, F. (2004). U-Pb age, setting and tectonic significance of the anorthosite-mangerite-charnockite-
2 698 granite suite, Lofoten-Vesterålen, Norway. *Journal of Petrology*, 56, 2081–2097.
3
4 699 Costa, M. M., Neiva, A. M. R., Azevedo, M. R., & Corfu, F. (2014). Distinct sources for syntectonic
5 700 Variscan granitoids: Insights from the Aguiar da Beira region, Central Portugal. *Lithos*, 196–197,
6 701 83–98. <https://doi.org/10.1016/j.lithos.2014.02.023>
7
8 702 Croudace, I. W. & Gilligan, J. (1990). Versatile and accurate trace element determinations in iron-rich
9 703 and other geological samples using X-ray fluorescence analysis. *X-ray Spectrometry*, 19, 117–123.
10
11 704 Croudace, I. W. & Thorpe, O. W. (1988). A low dilution, wavelength dispersive X-ray fluorescence
12 705 procedure for the analysis of archaeological rock artefacts. *Archaeometry*, 30, 227–236.
13
14 706 Cruz, C., Sant’Ovaia, H., & Noronha, F. (2020). Magnetic mineralogy of variscan granites from northern
15 707 Portugal: An approach to their petrogenesis and metallogenic potential. *Geologica Acta*, 18.
16 708 <https://doi.org/10.1344/GeologicaActa2020.18.5>
17
18 709 Davis, D. W., Blackburn, C. E. & Krogh, T. E. (1982). Zircon U–Pb ages from the Wabigoon. Manitou
19 710 Lakes Region, Wabigoon Subprovince, northwest Ontario. *Canadian Journal of Earth Sciences*, 19,
20 711 254–266.
21
22 712 De Paolo, D. J. (1981). Trace element and isotopic effects of combined wall rock assimilation and
23 713 fractional crystallization. *Earth and Planetary Science Letters*, 53, 189–202.
24
25 714 Dias, G., Leterrier, J., Mendes, A., Simões, P. P., & Bertrand, J. M. (1998). U-Pb zircon and monazite
26 715 geochronology of post-collisional Hercynian granitoids from the Central Iberian Zone (Northern
27 716 Portugal). *Lithos*, 45(1–4), 349–369. [https://doi.org/10.1016/S0024-4937\(98\)00039-5](https://doi.org/10.1016/S0024-4937(98)00039-5)
28
29 717 Dias, G., Simões, P. P., Ferreira, N. & Leterrier, J. (2002). Mantle and crustal sources in genesis of late-
30 718 Hercynian granitoids (NW Portugal). Geochemical and Sr-Nd isotopic constraints. *Gondwana
31 719 Research*, 5, 287–305.
32
33 720 Dias, R. & Coke, C. (2006). O funcionamento dos grandes acidentes crustais no controlo da génese e
34 721 instalação das rochas graníticas na Zona Centro Ibérica. In Dias, R., Araújo, A., Terrinha, P.,
35 722 Kullberg, J. (Eds.), *Geologia de Portugal no contexto da Ibéria* (pp. 1231–1234). Évora: Universidade
36 723 de Évora.

- 1 724 Didier, J. & Barbarin, B. (1991). The different types of enclaves in granites - Nomenclature. In Didier, J.
2
3 725 & Barbarin, B. (Eds.), *Enclaves in Granite Petrology. Developments in Petrology*, vol. 13 (pp. 19–
4
5 726 23). Amsterdam: Elsevier.
- 6
7 727 Ding, J., Han, C., Xiao, W., Wang, Z., & Song, D. (2017). Geochronology, geochemistry and Sr-Nd
8 728 isotopes of the granitic rocks associated with tungsten deposits in Beishan district, NW China,
9
10 729 Central Asian Orogenic Belt: Petrogenesis, metallogenetic and tectonic implications. *Ore Geology
11 Reviews*, 89, 441–462. <https://doi.org/10.1016/j.oregeorev.2017.06.018>
- 12
13 730 Feng, C., Wang, H., Xiang, X., & Zhang, M. (2018). Late Mesozoic granite-related W–Sn mineralization
14 731 in the northern Jiangxi region, SE China: A review. *Journal of Geochemical Exploration*, 195, 31–
15
16 732 48. <https://doi.org/10.1016/j.gexplo.2018.06.008>
- 17
18 733 Ferreira, N., Iglesias, M., Noronha, F., Pereira, E., Ribeiro, A. & Ribeiro, M. L. (1987). Granitóides da
19
20 734 zona Centro-Ibérica e seu enquadramento geodinâmico. In Bea, F., Carmina, A., Gonzalo, J.C., Plaza,
21
22 735 M.L., Rodrigues, J.M.L. (Eds.), *Geología de los granitoids y rocas asociadas del Macizo Hespérico,*
23
24 736 *Libro Homenagem a L.C.G. Figueirola* (pp. 37–53). Madrid: Editorial Rueda.
- 25
26
27 737 Förster, H.-J. & Romer, R. L. (2010). Carboniferous magmatism. In Linnemann, U., Romer, R. L. (Eds.),
28
29 738 *The pre-Mesozoic Geology of Saxo-Thuringia – From the Cadomian Active Margin to the Variscan
30 739 Orogen* (pp. 287–308). Stuttgart: Schweizerbart Science Publishers.
- 31
32 740 Frost, B. R., & Frost, C. D. (2008). A geochemical classification for feldspathic igneous rocks. *Journal of
33 741 Petrology*, 49(11), 1955–1969. <https://doi.org/10.1093/petrology/egn054>
- 34
35 742 Garcia-Arias, M., & Stevens, G. (2017). Phase equilibrium modelling of granite magma petrogenesis: B.
36
37 743 An evaluation of the magma compositions that result from fractional crystallization. *Lithos*, 277,
38
39 744 109–130. <https://doi.org/10.1016/j.lithos.2016.09.027>
- 40
41 745 Gioncada, A., Mazzuoli, R. & Milton, A. J. (2005). Magma mixing at Lipari (Aeolian Islands, Italy):
42
43 746 Insights from textural and compositional features of phenocrysts. *Journal of Volcanology and
44 747 Geothermal Research*, 145, 97–118.
- 45
46
47 748 Gomes, M. E. P., & Neiva, A. M. R. (2002). Petrogenesis of tin-bearing granites from Ervedosa, northern
48
49 749 Portugal: The importance of magmatic processes. *Chemie Der Erde*, 62(1), 47–72.
- 50
51 750 <https://doi.org/10.1078/0009-2819-00002>
- 52
53
54
55
56
57
58
59
60
61
62
63
64
65

- 1 752 Gomes, M. E. P., Teixeira, R. J. S., Neiva, A. M. R., & Corfu, F. (2014). Geoquímica e geocronologia
2 753 dos granitóides da região de Bemposta-Picote, Nordeste de Portugal. *Comunicações Geológicas*,
3 754 101, 115–118.
- 4 755 Gutiérrez-Alonso, G., Fernández-Suárez, J., López-Carmona, A., & Gärtner, A. (2018). Exhuming a cold
5 756 case: The early granodiorites of the northwest Iberian Variscan belt-A Visean magmatic flare-up?
6 757 *Lithosphere*, 10(2), 194–216. <https://doi.org/10.1130/L706.1>
- 7 758 Harris, N. B. W., Pearce J. A. & Tindle A.G. (1986). Geochemical characteristics of collision zone
8 759 magmatism. In Coward, M. P. & Ries A. C. (1986). Collision Tectonics (Special Publication 19, pp.
9 760 67-81). London: The Geological Society of London.
- 10 761 Henderson, P. (1984). Chapter 1 - General Geochemical Properties and Abundances of the Rare Earth
11 762 Elements. In P. B. T.-D. in G. Henderson (Ed.), *Rare Earth Element Geochemistry* (Vol. 2, pp. 1–
12 763 32). Elsevier. [https://doi.org/https://doi.org/10.1016/B978-0-444-42148-7.50006-X](https://doi.org/10.1016/B978-0-444-42148-7.50006-X)
- 13 764 Hoefs, J. & Emmermann, R. (1983). The oxygen isotopic composition of Hercynian granites and pre-
14 765 Hercynian gneisses from the Schwarzwald, SW Germany. *Contributions to Mineralogy and*
15 766 *Petrology*, 83, 320–329.
- 16 767 Hoefs, J. (2009). *Stable Isotope Geochemistry, 6th edition*. Berlin Heidelberg: Springer-Verlag,
- 17 768 Holtz, F. & Barbey, P. (1991). Genesis of peraluminous granites II. Mineralogy and chemistry of the
18 769 Tourem complex (northern Portugal). Sequential melting vs. restite unmixing. *Journal of Petrology*
19 770 32, 959–978.
- 20 771 Huang, L.-C., & Jiang, S.-Y. (2014). Highly fractionated S-type granites from the giant Dahutang
21 772 tungsten deposit in Jiangnan Orogen, Southeast China: Geochronology, petrogenesis and their
22 773 relationship with W-mineralization. *Lithos*, 202–203, 207–226.
- 23 774 <https://doi.org/10.1016/j.lithos.2014.05.030>
- 24 775 Jaffey, A. H., Flynn, K. F., Glendenin, L. E., Bentley, W. C., & Essling, A. M. (1971). Precision
25 776 measurement of half-lives and specific activities of U235 and U238. *Physical Review C*, 4(5),
26 777 1889–1906. <https://doi.org/10.1103/PhysRevC.4.1889>
- 27 778 Jiang, S., Peng, N., Huang, L., Xu, Y., Zhan, G., & Dan, X. (2015). Geological characteristic and ore
28 779 genesis of the giant tungsten deposits from the Dahutang ore-concentrated district in northern
29 780 Jiangxi Province. *Yanshi Xuebao/Acta Petrologica Sinica*, 31(3), 639–655.

- 1 781 Jung, S. & Pfänder, J. A. (2007). Source composition and melting temperatures of orogenic granitoids:
2 782 constrains from CaO/Na₂O, Al₂O₃/TiO₂ and accessory mineral saturation thermometry. *European*
3 783 *Journal of Mineralogy*, 19, 859–870.
4
5 784 Krogh, T. E. (1973). A low contamination method for hydrothermal decomposition of zircon and
6 785 extraction of U and Pb for isotopic age determination. *Geochimica et Cosmochimica Acta*, 37, 485–
7
8 786 494.
9
10 787 Krogh, T. E. (1982). Improved accuracy of U–Pb zircon ages by creation of more concordant systems
11 788 using an air abrasion technique. *Geochimica et Cosmochimica Acta*, 46, 637–649.
12
13 789 La Roche, H., Letterier, J., Grand Claude, P. & Marchal, M. (1980). A classification of volcanic and
14 790 plutonic rocks using R₁-R₂ diagrams and major elements analyses – its relationships with current
15 791 nomenclature. *Chemical Geology*, 29, 183–210.
16
17 792 Le Maitre, R., Streckeisen, A., Zanettin, B., Le Bas, M., Bonin, B., & Bateman, P. (Eds.). (2002). *Igneous*
18 793 *Rocks: A Classification and Glossary of Terms: Recommendations of the International Union of*
19 794 *Geological Sciences Subcommission on the Systematics of Igneous Rocks* (2nd ed.). Cambridge:
20
21 795 Cambridge University Press. doi:10.1017/CBO9780511535581
22
23 796 Ledru, P., Courrioux, G., Dallain, C., Lardeaux, J.-M., Montel, J.-M., Vanderhaeghe, O. & Vitel, G.
24
25 797 (2001). The Velay dome (French Massif Central): melt generation and granite emplacement during
26 798 orogenic evolution. *Tectonophysics*, 342, 207–227.
27
28 799 Lehmann, B. (1990). *Metallogeny of tin. Lecture Notes in Earth Sciences*. Berlin: Springer-Verlag.
29
30 800 Li, C., Yan, J., Yang, C., Song, C.-Z., Wang, A.-G., & Zhang, D.-Y. (2020). Generation of leucogranites
31 801 via fractional crystallization: A case study of the Jurassic Bengbu granite in the southeastern North
32 802 China Craton. *Lithos*, 352–353. <https://doi.org/10.1016/j.lithos.2019.105271>
33
34 803 Liew, T. C. & Hofmann, A. W. (1988). Precambrian crustal components, plutonic associations, plate
35 804 environment of the Hercynian Fold Belt of Central Europe: indications from a Nd and Sr study.
36
37 805 *Contributions to Mineralogy and Petrology*, 98, 129–138.
38
39 806 Liu, Y., Zhang, L., Mo, X., Santosh, M., Dong, G., & Zhou, H. (2020). The giant tin polymetallic
40 807 mineralization in southwest China: Integrated geochemical and isotopic constraints and
41 808 implications for Cretaceous tectonomagmatic event. *Geoscience Frontiers*.
42
43 809 <https://doi.org/10.1016/j.gsf.2020.01.007>

- 1 810 London, D., Černý, P., Loomis, J. L. & Pan, J. L. (1990). Phosphorus in alkali feldspars of rare-element
2 811 granitic pegmatites. *American Mineralogist*, 28, 771–786.
- 3 812 London, D., Wolf, M. B., Morgan VI, G. B., & Garrido, M. G. (1999). Experimental silicate-phosphate
4 813 equilibria in peraluminous granitic magmas, with a case study of the Alburquerque batholith at Tres
5 814 Arroyos, Badajoz, Spain. *Journal of Petrology*, 40(1), 215–240.
6
7 815 <https://doi.org/10.1093/petroj/40.1.215>
- 8
9 816 Ludwig, K. R. (1999). Isoplot/Ex version 2.03. *A geochronological toolkit for Microsoft Excel*. Berkeley
10 817 Geochronology under Special Publication, vol. 1. 43 pp.
- 11
12 818 Martins, H. C. B., Sant’Ovaia, H., & Noronha, F. (2013). Late-Variscan emplacement and genesis of the
13 819 Vieira do Minho composite pluton, Central Iberian Zone: Constraints from U–Pb zircon
14 820 geochronology, AMS data and Sr–Nd–O isotope geochemistry. *Lithos*, 162–163, 221–235.
15
16 821 <https://doi.org/https://doi.org/10.1016/j.lithos.2013.01.001>
- 17
18 822 Martins, H. C. B., Sant’Ovaia, H., Noronha, F. (2009). Genesis and emplacement of felsic Variscan
19 823 plutons within a deep crustal lineation, the Penacova-Régua-Verín fault: An integrated geophysics and
20 824 geochemical study (NW Iberian Peninsula). *Lithos*, 111, 142–155.
- 21
22 825 Merino Martínez, E., Villaseca, C., Orejana, D., Pérez-Soba, C., Belousova, E., & Andersen, T. (2014).
23 826 Tracing magma sources of three different S-type peraluminous granitoid series by in situ U-Pb
24 827 geochronology and Hf isotope zircon composition: The Variscan Montes de Toledo batholith
25 828 (central Spain). *Lithos*, 200–201(1), 273–298. <https://doi.org/10.1016/j.lithos.2014.04.013>
- 26
27 829 Miller, C. F., Hanchar, J. M., Wooden, J. L., Bennett, V. C., Harrison, T. M., Wark, D. A., Foster, D. A.
28 830 (1992). Source region of a granite batholiths: evidence from lower crustal xenoliths and inherited
29 831 accessory minerals. *Transactions of the Royal Society of Edinburgh: Earth Sciences*, 83, 49–62.
- 30
31 832 Miller, C. F., McDowell, S., Mapes, R. W. (2003). Hot and cold granites? Implications of zircon
32 833 saturation temperatures and preservation of inheritance. *Geology*, 31, 529–532.
- 33
34 834 Miller, C. F., Stoddard, E. F., Bradfish, L. J., & Dollase, W. A. (1981). Composition of plutonic
35 835 muscovite: genetic implications. *Canadian Mineralogist*, 19(1), 25–34.
- 36
37 836 Monier, G., Mergoil-Daniel, J., & Labernardiére, H. (1984). Générations successives de muscovites et
38 837 feldspaths potassiques dans les leucogranites du massif de Millevaches (Massif Central français).
39 838 *Bulletin de Minéralogie*, 107(1), 55–68. <https://doi.org/10.3406/bulmi.1984.7793>
- 40
41
42
43
44
45
46
47
48
49
50
51
52
53
54
55
56
57
58
59
60
61
62
63
64
65

- 1 839 Müller, A., Seltmann, R., Halls, C., Siebel, W., Dulski, P., Jeffries, T., Spratt, J., Kronz, A. (2006). The
2 840 magmatic evolution of the Land's End pluton, Cornwall, and associated pre-enrichment of metals. *Ore*
3 841 *Geology Reviews*, 28, 329–367.
4
5 842 Nachit, H., Razafimahafa, N., Stussi, J. M., & Carron, J. P. (1985). Composition chimique des biotites et
6 843 typologie magmatique des granitoides. *Comptes Rendus de l'Académie Des Sciences, Paris, Serie*
7 844 *II*, 301(11), 813–818.
8
9 845 Nash, W. P., & Crecraft, H. R. (1985). Partition coefficients for trace elements in silicic magmas.
10
11 846 *Geochimica et Cosmochimica Acta*, 49(11), 2309–2322. [https://doi.org/10.1016/0016-7037\(85\)90231-5](https://doi.org/10.1016/0016-7037(85)90231-5)
12
13 847
14
15 848 Neiva, A. M. R. & Gomes, M.E.P. (2001). Diferentes tipos de granitos e seus processos petrogenéticos:
16
17 849 granitos hercínicos portugueses. *Memórias da Academia das Ciências de Lisboa*, 31, 53–95.
18
19 850 Neiva, A. M. R. & Ramos, J. M. F. (2010). Geochemistry of granite aplite-pegmatite sills and
20
21 851 petrogenetic links with granites, Guarda-Belmonte area, central Portugal. *European Journal of*
22
23 852 *Mineralogy*, 22(6), 837–854.
24
25
26
27
28
29 853 Neiva, A. M. R. (1984). Geochemistry of tin-bearing granitic rocks. *Chemical Geology*, 43(3–4), 241–
30
31 854 256. [https://doi.org/10.1016/0009-2541\(84\)90052-4](https://doi.org/10.1016/0009-2541(84)90052-4)
32
33 855 Neiva, A. M. R. (1994). Dating and geochemistry of tin-bearing granitic rocks and their minerals from
34
35 856 NE of Gerez mountain, Northern Portugal. *Boletín de la Sociedad Española de Mineralogía*, 17, 65–
36
37 857 82.
38
39 858 Neiva, A. M. R. (1998). Geochemistry of highly peraluminous granites and their minerals between Douro
40
41 859 and Tamega valleys, northern Portugal. *Chemie der Erde*, 58, 161–184.
42
43 860 Neiva, A. M. R. (2002). Portuguese granites associated with Sn-W and Au mineralizations. *Bulletin of the*
44
45 861 *Geological Society of Finland*, 74, 79–101.
46
47 862 Neiva, A. M. R., Silva, P. B., Corfu, F., & Ramos, J. M. F. (2011a). Sequential melting and fractional
48
49 863 crystallization: Granites from Guarda-Sabugal area, central Portugal. *Geochemistry*, 71(3), 227–
50
51 864 245. <https://doi.org/10.1016/j.chemer.2011.06.002>
52
53 865 Neiva, A. M. R., Silva, P. B., Ramos, J. M. F. (2011b). Geochemistry of granitic aplite-pegmatite veins
54
55 866 and sills and their minerals from the Sabugal area, central Portugal. *Neues Jahrbuch für Mineralogie*,
56
57 867 189(1), 49–74.
58
59
60
61
62
63
64
65

- 1 868 Neiva, A. M. R., Williams, I. S., Ramos, J. M. F., Gomes, M. E. P., Silva, M. M. V. G., & Antunes, I. M.
2
3 869 H. R. (2009). Geochemical and isotopic constraints on the petrogenesis of Early Ordovician
4
5 870 granodiorite and Variscan two-mica granites from the Gouveia area, central Portugal. *Lithos*,
6
7 871 111(3–4), 186–202. <https://doi.org/10.1016/j.lithos.2009.01.005>
8
9 872 Nekvasil, H. (1992). Ternary feldspar crystallization in high-temperature felsic magmas. *American
10
11 Mineralogist*, 77, 592–604.
12
13 874 Nguyen, T. A., Yang, X., Thi, H. V., Liu, L., & Lee, I. (2019). Piaoac Granites Related W-Sn
14
15 875 Mineralization, Northern Vietnam: Evidences from Geochemistry, Zircon Geochronology and Hf
16
17 876 Isotopes. *Journal of Earth Science*, 30(1), 52–69. <https://doi.org/10.1007/s12583-018-0865-6>
18
19 877 Oliveira, J., Pereira, E., Piçarra, J., Young, T. & Romano, M. (1992). O Paleozóico Inferior de Portugal:
20
21 878 síntese da estratigrafia e da evolução paleogeográfica. In Gutiérrez Marco, J.C., Saavedra, J., Rábano,
22
23 879 I. (Eds.), Paleozóico Inferior de Ibero-América (pp. 359–375). Badajoz: Universidad de Extremadura.
24
25 880 Otamendi, J. E., Nullo, F. E., Patiño Douce, A. E., Fagiano, M. (1998). Geology, mineralogy and
26
27 881 geochemistry of syn-orogenic anatexitic granites from the Achiras Complex, Córdoba, Argentina:
28
29 882 some petrogenetic and geodynamic implications. *Journal of South American Earth Sciences*, 11(4),
30
31 883 407–423.
32
33 884 Pan, X., Hou, Z., Zhao, M., Chen, G., Rao, J., Li, Y., Wei, J., & Ouyang, Y. (2018). Geochronology and
34
35 885 geochemistry of the granites from the Zhuxi W-Cu ore deposit in South China: Implication for
36
37 886 petrogenesis, geodynamical setting and mineralization. *Lithos*, 304–307, 155–179.
38
39 887 <https://doi.org/10.1016/j.lithos.2018.01.014>
40
41 888 Pearce, J. A., Harris, N. B. W., Tindle, A. G. (1984). Trace element discrimination diagrams for the
42
43 889 tectonic interpretation of granitic rocks. *Journal of Petrology* 25, 956–983.
44
45 890 Pereira, M. F., Castro, A., Fernández, C., & Rodríguez, C. (2018). Multiple Paleozoic magmatic-orogenic
46
47 891 events in the Central Extremadura batholith (Iberian Variscan belt, Spain). *Journal of Iberian
48
49 892 Geology*, 44(2), 309–333. <https://doi.org/10.1007/s41513-018-0063-5>
50
51 893 Pin, C., & Santos Zalduogui, J. F. (1997). Sequential separation of light rare-earth elements, thorium and
52
53 894 uranium by miniaturized extraction chromatography: Application to isotopic analyses of silicate
54
55 895 rocks. *Analytica Chimica Acta*, 339(1–2), 79–89. [https://doi.org/10.1016/S0003-2670\(96\)00499-0](https://doi.org/10.1016/S0003-2670(96)00499-0)

- 1 896 Poitrasson, F., Chenery, S., & Bland, D. J. (1996). Contrasted monazite hydrothermal alteration
2 897 mechanisms and their geochemical implications. *Earth and Planetary Science Letters*, 145(1–4),
3 898 79–96. [https://doi.org/10.1016/s0012-821x\(96\)00193-8](https://doi.org/10.1016/s0012-821x(96)00193-8)
- 4 899 Qiu, Z., Yan, Q., Li, S., Wang, H., Tong, L., Zhang, R., Wei, X., Li, P., Wang, L., Bu, A., Bu, A., & Yan,
5 900 L. (2017). Highly fractionated Early Cretaceous I-type granites and related Sn polymetallic
6 901 mineralization in the Jinkeng deposit, eastern Guangdong, SE China: Constraints from
7 902 geochronology, geochemistry, and Hf isotopes. *Ore Geology Reviews*, 88, 718–738.
8 903 <https://doi.org/10.1016/j.oregeorev.2016.10.008>
- 9 904 Rieder, M., Cavazzini, G., D'Yakonov, Y. S., Frank-Kamenetskii, V. A., Gottardi, G., Guggenheim, S.,
10 905 Koval', P. V., Müller, G., Neiva, A. M. R., Radoslovich, E. W., Robert, J. L., Sassi, F. P., Takeda,
11 906 H., Weiss, Z., & Wones, D. R. (1998). Nomenclature of the micas. *Canadian Mineralogist*, 36(3),
12 907 905–912. <https://doi.org/10.1180/minmag.1999.063.2.13>
- 13 908 Roda-Robles, E., Villaseca, C., Pesquera, A., Gil-Crespo, P. P., Vieira, R., Lima, A., & Garate-Olave, I.
14 909 (2018). Petrogenetic relationships between Variscan granitoids and Li-(F-P)-rich aplite-pegmatites
15 910 in the Central Iberian Zone: Geological and geochemical constraints and implications for other
16 911 regions from the European Variscides. *Ore Geology Reviews*, 95, 408–430.
17 912 <https://doi.org/10.1016/j.oregeorev.2018.02.027>
- 18 913 Romer, R. L., & Kroner, U. (2016). Phanerozoic tin and tungsten mineralization-Tectonic controls on the
19 914 distribution of enriched protoliths and heat sources for crustal melting. *Gondwana Research*, 31,
20 915 60–95. <https://doi.org/10.1016/j.gr.2015.11.002>
- 21 916 Romer, R. L., Förster, H.-J., & Hahne, K. (2012). Strontium isotopes — A persistent tracer for the
22 917 recycling of Gondwana crust in the Variscan orogen. *Gondwana Research*, 22(1), 262–278.
23 918 <https://doi.org/10.1016/j.gr.2011.09.005>
- 24 919 Ruiz, C., Fernández-Leyva, C., & Locutura, J. (2008). Geochemistry, geochronology and mineralisation
25 920 potential of the granites in the Central Iberian Zone: The Jalama batholith. *Chemie Der Erde*, 68(4),
26 921 413–429. <https://doi.org/10.1016/j.chemer.2006.11.001>
- 27 922 Schärer, U. (1984). The effect of initial ^{230}Th disequilibrium on young U-Pb ages: the Makalu case,
28 923 Himalaya. *Earth and Planetary Science Letters*, 67(2), 191–204. [https://doi.org/10.1016/0012-821X\(84\)90114-6](https://doi.org/10.1016/0012-821X(84)90114-6)

- 1 925 Silva, A. F., Rebelo, J. A. & Ribeiro, M. L. (1989). Notícia explicativa da Folha 11-C (Torre de
2 Moncorvo). Serviços Geológicos de Portugal, Lisboa.
3
4 927 Silva, A. F., Rebelo, J. A., Santos, A.J., Cardoso, F., Ribeiro, M.L., Ribeiro, A., Cabral, J. & Estagiários
5
6 928 da F.C.L. (1987/88). Carta Geológica de Portugal à escala 1:50 000 (Folha 11-C, Torre de Moncorvo).
7
8 929 Serviços Geológicos de Portugal.
9
10 930 Simons, B., Andersen, J. C. Ø., Shail, R. K., & Jenner, F. E. (2017). Fractionation of Li, Be, Ga, Nb, Ta,
11
12 931 In, Sn, Sb, W and Bi in the peraluminous Early Permian Variscan granites of the Cornubian
13
14 932 Batholith: Precursor processes to magmatic-hydrothermal mineralisation. *Lithos*, 278–281, 491–
15
16 933 512. <https://doi.org/10.1016/j.lithos.2017.02.007>
17
18 934 Simons, B., Shail, R. K., & Andersen, J. C. O. (2016). The petrogenesis of the Early Permian Variscan
19
20 935 granites of the Cornubian Batholith: Lower plate post-collisional peraluminous magmatism in the
21
22 936 Rhenohercynian Zone of SW England. *Lithos*, 260, 76–94.
23
24 937 <https://doi.org/10.1016/j.lithos.2016.05.010>
25
26 938 Smith, W. D., Darling, J. R., Bullen, D. S., Lasalle, S., Pereira, I., Moreira, H., Allen, C. J., & Tapster, S.
27
28 939 (2019). Zircon perspectives on the age and origin of evolved S-type granites from the Cornubian
29
30 940 Batholith, Southwest England. *Lithos*, 336–337, 14–26. <https://doi.org/10.1016/j.lithos.2019.03.025>
31
32 941 Sousa, L. (2000). *Estudo da fracturação e das carcterísticas físico-mecânicas de granitos da região de*
33
34 942 *Trás-os-Montes com vista à sua utilização como rocha ornamental*. Unpublished PhD thesis,
35
36 943 University of Trás-os-Montes e Alto Douro, 479 p.
37
38 944 Stacey, J. S., & Kramers, J. D. (1975). Approximation of terrestrial lead isotope evolution by a two-stage
39
40 945 model. *Earth and Planetary Science Letters*, 26(2), 207–221. [https://doi.org/10.1016/0012-821X\(75\)90088-6](https://doi.org/10.1016/0012-821X(75)90088-6)
41
42 946
43
44 947 Steiger, R. H., & Jäger, E. (1977). Subcommission on geochronology: Convention on the use of decay
45
46 948 constants in geo- and cosmochronology. *Earth and Planetary Science Letters*, 36(3), 359–362.
47
48 949 [https://doi.org/10.1016/0012-821X\(77\)90060-7](https://doi.org/10.1016/0012-821X(77)90060-7)
49
50 950 Sylvester, A. G. (1998). Magma mixing, structure, and re-evaluation of the emplacement mechanism of
51
52 951 Vrådal pluton, central Telemark, southern Norway. *Norsk Geologisk Tidsskrift*, (78), 259–276.
53
54 952 Tassinari, C. C. G., Medina, J., Pinto, M. S. (1995). Rb-Sr and Sm-Nd geochronology and isotope
55
56 953 geochemistry of Central Iberian metasedimentary rocks (Portugal). *Geologie en Mijnbouw*, 75, 69–79.

- Taylor, S. R. & McLennan, S. M. (1985). *The continental crust: its composition and evolution*. Carlton: Blackwell Scientific Publication.

Teixeira, R. J. S. (2008). *Mineralogia, petrologia e geoquímica dos granitos e seus encraves da região de Carrazeda de Ansiães*. Unpublished PhD thesis, University of Trás-os-Montes e Alto Douro, 430 p.

Teixeira, R. J. S., Coke, C., Dias, R. & Gomes, M. E. P. (2012b). U-Pb geochronology of detrital zircons from a metaconglomerate of the Formation of São Domingos (Group of Douro), Desejosa/Castanheiro do Sul, Northern Portugal. *European Mineralogical Conference - Vol. 1*, 442.

Teixeira, R. J. S., Coke, C., Gomes, M. E. P. & Corfu, F. (2013a). ID-TIMS U-Pb ages of Tremadocian-Floian ash-fall tuff beds from Marão and Eucísia areas, Northern Portugal. *William Smith Meeting 2013: The First Century of Isotope Geochronology: the Legacy of Frederick Soddy & Arthur Holmes – Abstract Book*, 152-154.

Teixeira, R. J. S., Coke, C., Gomes, M. E. P., Dias, R. & Martins, L. O. (2013b). U-Pb geochronology of detrital zircons from metasedimentary rocks from Formation of Desejosa, Serra do Marão, Portugal. (Goldschmidt Conference Abstract). *Mineralogical Magazine*, 77(5), 2318.

Teixeira, R. J. S., Neiva, A. M. R., Gomes, M. E. P., Corfu, F., Cuesta, A., & Croudace, I. W. (2012a). The role of fractional crystallization in the genesis of early syn-D 3, tin-mineralized Variscan two-mica granites from the Carrazeda de Ansiães area, northern Portugal. *Lithos*, 153, 177–191.
<https://doi.org/10.1016/j.lithos.2012.04.024>

Teixeira, R. J. S., Neiva, A. M. R., Silva, P. B., Gomes, M. E. P., Andersen, T., & Ramos, J. M. F. (2011). Combined U-Pb geochronology and Lu-Hf isotope systematics by LAM-ICPMS of zircons from granites and metasedimentary rocks of Carrazeda de Ansiães and Sabugal areas, Portugal, to constrain granite sources. *Lithos*, 125(1–2), 321–334. <https://doi.org/10.1016/j.lithos.2011.02.015>

Teixeira, R. J. S., Urbano, E. E. M. C., Gomes, M. E. P., Meireles, C. A., Corfu, F., Santos, J. F., Azevedo, M. R., & Sá, A. A. (2015). Interbedded quartz-muscovite layers in the ferriferous quartzites of the Lower Ordovician deposits of Moncorvo synclinorium (NE Portugal): An example of volcanogenic metasedimentary deposits?. *Comunicações Geológicas*, 102 (Special Is), 31–39.

Tischendorf, G., Gottesmann, B., Foster, H-J. & Trumbull, R. B. (1997). On Li-bearing micas: estimating Li from electron microprobe analyses and an improved diagram for graphical representation. *Mineralogical Magazine*, 61, 809–834.

- 1 983 Valle Aguado, B., Azevedo, M. R., Schaltegger, U., Martínez Catalán, J. R., & Nolan, J. (2005). U-Pb
2 984 zircon and monazite geochronology of Variscan magmatism related to syn-convergence extension
3 985 in Central Northern Portugal. *Lithos*, 82(1-2 SPEC. ISS.), 169–184.
4
5 986 <https://doi.org/10.1016/j.lithos.2004.12.012>
6
7 987 Villaseca, C., Barbero, L., Rogers, G. (1998). Crustal origin of Hercynian peraluminous granitic
8 988 batholiths of Central Spain: petrological, geochemical and isotopic (Sr, Nd) constraints. *Lithos*, 43,
9
10 989 55–79.
11
12 990 Villaseca, C., Downes, H., Pin, C., Barbero, L. (1999). Nature and Composition of the Lower Continental
13 991 Crust in Central Spain and the Granulite–Granite Linkage: Inferences from Granulitic Xenoliths.
14 992 [Journal of Petrology](https://doi.org/10.1016/j.jpetro.1999.0001), 40(10), 1465–1496.
15
16 993 Villaseca, C., Merino, E., Oyarzun, R., Orejana, D., Pérez-Soba, C., & Chicharro, E. (2014). Contrasting
17 994 chemical and isotopic signatures from Neoproterozoic metasedimentary rocks in the Central Iberian
18 995 Zone (Spain) of pre-Variscan Europe: Implications for terrane analysis and Early Ordovician
19 996 magmatic belts. *Precambrian Research*, 245, 131–145.
20
21 997 <https://doi.org/10.1016/j.precamres.2014.02.006>
22
23 998 Villaseca, C., Pérez-Soba, C., Merino, E., Orejana, D., López-García, J. A., & Billstrom, K. (2008).
24
25 999 Contrasting crustal sources for peraluminous granites of the segmented Montes de Toledo Batholith
26 1000 (Iberian Variscan Belt). *Journal of Geosciences*, 53(3–4), 263–280.
27
28 1001 <https://doi.org/10.3190/jgeosci.035>
29
30 1002 Wang, F., Bagas, L., Jiang, S., & Liu, Y. (2017). Geological, geochemical, and geochronological
31 1003 characteristics of Weilasituo Sn-polymetal deposit, Inner Mongolia, China. *Ore Geology Reviews*,
32 1004 80, 1206–1229. <https://doi.org/10.1016/j.oregeorev.2016.09.021>
33
34 1005 Wang, L.-X., Ma, C.-Q., Zhang, C., Zhang, J.-Y., & Marks, M. A. W. (2014). Genesis of leucogranite by
35 1006 prolonged fractional crystallization: A case study of the Mufushan complex, South China. *Lithos*,
36 1007 206–207(1), 147–163. <https://doi.org/10.1016/j.lithos.2014.07.026>
37
38 1008 Wasserburg, G. J., Jacobsen, S. B., De Paolo, D. J., McCulloch, M. T. & Wen, T. (1981). Precise
39 1009 determination of Sm/Nd ratios, Sm and Nd isotopic abundances in standard solutions. *Geochimica et
40 1010 Cosmochimica Acta*, 45, 2311–2323.

- 1 1011 Watson, E. B. & Harrison, T. M. (1983). Zircon saturation revisited: temperature and composition effects
2 1012 in a variety of crustal magma types. *Earth and Planetary Science Letters*, 64, 295–304.
3
4 1013 Williamson, B. J., Shaw, A., Downes, H. & Thrillwall, M.F. (1996). Chemical constraints on the genesis
5 1014 of Hercynian two-mica leucogranites from the Massif Central. *Chemical Geology*, 127, 25–42.
6
7 1015 Xu, B., Jiang, S.-Y., Wang, R., Ma, L., Zhao, K.-D., & Yan, X. (2015). Late Cretaceous granites from the
8 1016 giant Dulong Sn-polymetallic ore district in Yunnan Province, South China: Geochronology,
9 1017 geochemistry, mineral chemistry and Nd-Hf isotopic compositions. *Lithos*, 218–219, 54–72.
10 1018 https://doi.org/10.1016/j.lithos.2015.01.004
11
12 1019 Yurimoto, H., Duke, E. F., Papike, J.J. & Shearer, C. K. (1990). Are discontinuous chondrite-normalized
13 1020 REE patterns in pegmatitic granitic systems the results of monazite fractionation? *Geochimica et*
14 1021 *Cosmochimica Acta*, 54, 2141–2145.
15
16 1022 Zhang, L.-X., Wang, Q., Zhu, D.-C., Li, S.-M., Zhao, Z.-D., Zhang, L.-L., Chen, Y., Liu, S.-A., Zheng,
17 1023 Y.-C., Wang, R., Wang, R., & Liao, Z.-L. (2019). Generation of leucogranites via fractional
18 1024 crystallization: A case from the Late Triassic Luoza batholith in the Lhasa Terrane, southern Tibet.
19 1025 *Gondwana Research*, 66, 63–76. https://doi.org/10.1016/j.gr.2018.08.008
20
21 1026
22
23 1027
24
25 1028
26
27 1029
28
29 1030
30
31 1031
32
33 1032
34
35 1033
36
37 1034
38
39 1035
40
41 1036
42
43 1037
44
45 1038
46
47 1039
48
49
50
51
52
53
54
55
56
57
58
59
60
61
62
63
64
65

1 1040 **Table captions**
2
3 1041 **Table 1.** Geological, petrographic and geochemical characteristics of granites G7 - G10 from Carrazeda
4
5 1042 de Ansiães area, northern Portugal.
6
7 1043 **Table 2.** Average modal compositions and average whole rock chemical analyses in wt.% and trace
8
9 1044 elements in ppm of granites G7 - G10 from Carrazeda de Ansiães area, northern Portugal.
10
11 1045 **Table 3.** U-Pb data of zircon and monazite from granites G7 - G10 of Carrazeda de Ansiães area,
12
13 1046 northern Portugal.
14
15 1047
16
17 1048
18
19 1049 **Supplemental electronic table captions**
20
21 1050 **Supplemental electronic data Table 1.** Representative analyses of rare earth elements (ppm) of granites
22
23 1051 G7 - G10 from Carrazeda de Ansiães area, northern Portugal.
24
25 1052 **Supplemental electronic data Table 2.** Whole rock Rb-Sr, Sm-Nd and oxygen isotopic values of
26
27 1053 granites G7 - G10 from Carrazeda de Ansiães area, northern Portugal.
28
29 1054 **Supplemental electronic data Table 3.** Average chemical analyses (EPMA) in wt.% and trace elements
30
31 1055 (laser ablation ICP-MS) in ppm of feldspars of granites G7 - G10 from Carrazeda de Ansiães area,
32
33 1056 northern Portugal.
34
35 1057 **Supplemental electronic data Table 4.** Average chemical analyses (EPMA) in wt.% and trace elements
36
37 1058 (laser ablation ICP-MS) in ppm of biotites and muscovites of granites G7 - G10 from Carrazeda de
38
39 1059 Ansiães area, northern Portugal.
40
41 1060 **Supplemental electronic data Table 5.** Electron microprobe analyses in wt.% and cations based on 6
42
43 1061 oxygens of ilmenites of granites G7 - G10 from Carrazeda de Ansiães area, northern Portugal.
44
45 1062 **Supplemental electronic data Table 6.** Results of the fractional crystallization modeling of granites G8,
46
47 1063 G9 and G10 from Carrazeda de Ansiães area, northern Portugal.
48
49 1064
50
51 1065
52
53 1066
54
55 1067
56
57 1068
58
59
60
61
62
63
64
65

1 1069 **Figure captions**
2
3
4
5 1071 **Fig. 1.** a) Distribution of Variscan syn- to post-kinematic granites from northern and central Portugal
6
7 1072 (Azevedo and Valle Aguado, 2006) and location of the Carrazeda de Ansiães area; b) Geological map
8
9 1073 of the area (after Silva et al., 1987/88). 1- metasedimentary formations of the Douro Group; 2- early
10
11 1074 syn-D₃ Variscan granites (Group I); G7- medium- to coarse-grained slightly porphyritic muscovite >
12
13 1075 biotite granite; G8- medium-grained porphyritic biotite ≈ muscovite granite; G9- Medium-grained
14
15 1076 porphyritic granite muscovite > biotite granite; G10- Medium-grained slightly porphyritic muscovite-
16
17 1077 dominant granite; 3- late syn-D₃ Variscan granites; 4- rhyolitic porphyry, aplite, pegmatite and quartz
18
19 1078 veins; 5- lamprophyre and microgabbro; 6- sedimentary cover; 7- geological contact; 8- fault; 9-
20
21 1079 probable fault; 10- sampling sites for U-Pb dating.
22
23
24
25
26 1080

27 1081 **Fig. 2.** a) Magmatic foliation in granite G9 defined by feldspar phenocrysts; b) Surmicaceous enclaves in
28
29 1082 granite G8, oriented parallel to the N55-60°W magmatic foliation; c) Magmatic foliation in granite G8
30
31 1083 defined by biotite. The quartz crystals of the matrix are only slightly deformed (photomicrograph in ×
32
33 1084 nicols); d) Round-shaped enclave of granite G7 in granite G8; e) Irregular-shaped tonalitic enclave in
34
35 1085 granite G8; f) Fine-grained monzogranite enclave, partially enclosing phenocrysts of the host granite
36
37 1086 G9; g) Microfracturing of plagioclase in granite G10. One of the microfractures is filled with quartz
38
39 1087 (photomicrograph in × nicols); h) Muscovite from G10 granite affected by a microfracture and micro-
40
41 1088 scale “kink” type folding. The microfracture extends to the adjacent plagioclase crystal, subdividing
42
43 1089 into multiple branches (photomicrograph in × nicols); i) BSE image of an isolated crystal of apatite
44
45 1090 from granite G9, with inclusions of zircon, monazite and ilmenite. Abbreviations: Ap-apatite, Bt-
46
47 1091 biotite, Ilm- ilmenite; Mcl- microcline, Ms- muscovite, Pl- plagioclase, Qtz- quartz and Zrn- zircon.
48
49
50 1092

51 1093 **Fig. 3.** Variation diagrams for whole rock major and trace element concentrations in granites G7 - G10
52
53 1094 from Carrazeda de Ansiães area. The samples of granite G7 define one trend, whereas granites G8, G9
54
55 1095 and G10 define a different trend. The samples richest in Rb of granite G7 reflect some metasomatic
56
57 1096 effects and, therefore, were not considered in the curvilinear regression.
58
59
60
61
62
63
64
65 1097

1 1098 **Fig. 4.** Average chondrite-normalized REE abundances for granites G7 - G10 from Carrazeda de Ansiães
2 1099 area, northern Portugal. Chondrite abundances from Taylor and McLennan (1985).
3
4
5
6

7 1101 **Fig. 5.** Ocean-ridge granite-normalized (ORG) diagram of Pearce et al. (1984) and Harris et al. (1986) for
8 1102 granites G7 - G10 from Carrazeda de Ansiães area, northern Portugal. The shaded area corresponds to
9
10
11 1103 syn-collisional granites from Harris et al. (1986).
12
13
14
15 1104
16 1105 **Fig. 6.** Concordia diagrams displaying the U-Pb data for zircon (white ellipses) and monazite (gray
17 1106 ellipses) for the four units of the suite, with error ellipses drawn at 2σ , and BSE images of isolated
18
19 1107 monazite crystals. The resorbed texture of the monazite from granite G8 (d) was probably the result of
20
21 1108 an alteration process, whereas in the subhedral monazite from granite G9 there is evidence of an
22
23 1109 inherited core (e).
24
25
26
27 1110
28 1111 **Fig. 7.** Diagram of $\epsilon_{\text{Nd}}{}_{320 \text{ Ma}}$ versus $(^{87}\text{Sr}/^{86}\text{Sr})_{320 \text{ Ma}}$ of granites G7 - G10 from Carrazeda de Ansiães area,
29
30 1112 northern Portugal. Results of field projections for (A) felsic peraluminous granulites (lower-crustal
31
32 1113 xenoliths; Villaseca et al., 1999); (B) metasediments from Beiras Group (Beetsma, 1995; Tassinari et
33
34 1114 al., 1996) and southern CIZ (Villaseca et al., 2014), (C) orthogneisses from the Spanish Central
35
36 1115 System (Villaseca et al., 1998), (D) pelitic peraluminous granulites (lower-crustal xenoliths; Villaseca
37
38 1116 et al., 1999), (E) metasediments from Douro Group (Teixeira et al., 2012) and northern CIZ (Villaseca
39
40 1117 et al., 1998, 2014) and (F) metasediments from Ordovician units of Central Iberian Zone and Galicia-
41
42 1118 Trás-os-Montes Zone and from Silurian units of Galicia-Trás-os-Montes (Beetsma, 1995).
43
44
45 1119
46 1120 **Fig. 8.** Whole rock Rb-Sr isochron diagram for granites G8, G9 and G10 from Carrazeda de Ansiães area,
47
48 1121 northern Portugal.
49
50
51 1122
52 1123 **Fig. 9.** Plots and trend lines of whole rock Sn versus Sn in: a) biotite and b) muscovite of series G8, G9
53
54 1124 and G10 from Carrazeda de Ansiães area, northern Portugal.
55
56
57
58
59
60
61
62
63
64
65
1125

1 1126 **Fig. 10.** Correlation of log Rb/Sr – log Sn for series G8, G9 and G10 from Carrazeda de Ansiães area,
2
3 1127 northern Portugal. Global reference fields from Lehman (1990).

4
5 1128
6
7 1129
8
9 1130 **Supplemental electronic figure captions**
10
11 1131
12
13 1132 **Supplemental electronic Fig. 1.** Variation diagrams for selected major and trace elements, showing trend
14
15 1133 lines for the differentiation series G8, G9 and G10.
16
17 1134
18
19 1135 **Supplemental electronic Fig. 2.** Variation diagrams of selected major and trace element abundances of:
20
21 1136 a) matrix microcline and b) matrix plagioclase plotted against the whole rock Fe₂O₃t abundance of
22
23 1137 granites G7 - G10 from Carrazeda de Ansiães area, northern Portugal, showing trend lines for
24
25 1138 differentiation series G8, G9 and G10.
26
27 1139
28
29 1140 **Supplemental electronic Fig. 3.** Variation diagrams of selected major and trace elements of: a) biotite, b)
30
31 1141 muscovite and c) ilmenite against the whole rock Fe₂O₃t abundance of granites G7 - G10 from
32
33 1142 Carrazeda de Ansiães area, northern Portugal, showing trend lines for differentiation series G8, G9
34
35 1143 and G10.
36
37 1144
38
39 1145 **Supplemental electronic Fig. 4.** Plot of modal quartz, K-feldspar, plagioclase and biotite of cumulate
40
41 1146 and calculated Sr, Ba and Rb concentrations in granites G8, G9 and G10 from Carrazeda de Ansiães
42
43 1147 area, northern Portugal versus the weight fraction (FR) of melt remaining during fractional
44
45 1148 crystallization and comparison of the measured (solid regression line) and calculated (dashed
46
47 1149 regression line) concentrations of Sr, Ba and Rb. The model supports fractional crystallization.
48
49
50
51
52
53
54
55
56
57
58
59
60
61
62
63
64
65

Table 1

Geological, petrographic and geochemical characteristics of granites G7 – G10 from Carrazeda de Ansiães area, northern Portugal

Granites / Location	Mineralogy	Texture and average dimensions for phenocrysts / Enclaves	Number, shape, size and deformation of the intrusions	Geochemical fingerprints	Source character and isotopes
<i>General features of granites G7 – G10</i>	Quartz, plagioclase, microperthitic microcline, biotite, some chlorite, muscovite, tourmaline, zircon, apatite, monazite, ilmenite, rutile and anatase.	Subhedral granular texture, containing feldspar phenocrysts.		Peraluminous and alkali-calcic.	Granites G7 and G8 are of S-type and result from the sequential partial melting of the same metasedimentary material.
<i>Granite G7</i> Along a WNW-ESE alignment, from Parambos/Carrazeda de Ansiães to Lousa.	Muscovite > biotite granite. Contains sillimanite.	Medium- to coarse-grained slightly porphyritic granite; up to 2.5 × 0.9 cm. Surmicaceous and metasedimentary xenoliths and “schlieren”.	Crops out as a 81 km ² WNW-ESE trending body that intruded Douro Group metasediments and partially surrounds the early syn-D ₃ granites G3, G4, G5 and G6. A N50–60°W magmatic foliation is defined by biotite and more rarely by feldspar phenocrysts. This granite is affected by a NNE-SSW fracture system.	ASI: 1.23 – 1.38 Normative corundum: 2.79 – 4.36 % ΣREE: 101.1 ppm	Age: 317.8 ± 0.5 Ma (⁸⁷ Sr/ ⁸⁶ Sr) _i = 0.7156 ± 0.0005 εNd _t = -8.5 δ ¹⁸ O = 11.35 – 11.62 ‰
<i>Granite G8</i> Around and W of Quinta das Vinhas, and S of Besteiros, to the S and centre of the area, respectively.	Biotite ≈ muscovite granite Contains sillimanite.	Medium-grained porphyritic granite; from 1 × 0.4 cm to 2.4 × 0.8 cm. Surmicaceous, metasedimentary xenoliths, monzogranite enclaves and granite G7 enclaves.	Three distinct bodies, one of 1.5 km ² in the centre of the area with a WNW-ESE elongation, and two of 0.85 km ² and 0.25 km ² in the S. This homogeneous granite type intruded Douro Group metasediments and partially surrounds granite G7, showing sharp and fault contacts locally filled with aplite. It has a magmatic N55–60°W foliation defined by oriented feldspar phenocrysts, biotite and, locally, by surmicaceous enclaves and xenoliths.	ASI: 1.22 – 1.39 Normative corundum: 2.85 – 4.39 % ΣREE: 286.9 ppm	Age: 316.8 ± 1.3 Ma (⁸⁷ Sr/ ⁸⁶ Sr) _i = 0.7155 ± 0.0007 εNd _t = -8.4 δ ¹⁸ O = 11.12 – 11.76 ‰
<i>Granite G9</i> Around Campelos and SW of Marzagão in the SW; SE of Fonte Longa in the centre and SE of Lousa in the SE of the area.	Muscovite > biotite granite. Contains sillimanite.	Medium-grained porphyritic granite; from 2.5 × 0.7 cm to 0.9 × 0.3 cm. Surmicaceous and metasedimentary xenoliths, “schlieren”, G7 granite enclaves.	A main body of 24 km ² , with an approximated NW-SW elongation, and a smaller body of 1 km ² in the SW. In the centre of the area there is another body of 1 km ² , and a fourth body of 2.5 km ² occurs to the SE of the area. This granite type intruded Douro Group metasediments and partially surrounds the early syn-D ₃ granites G3 and G5. This granite unit shows frequent sharp intrusive contacts with granite G7, but faulted contacts also occur. A N50–60°W magmatic foliation is defined by feldspar phenocrysts and biotite.	ASI: 1.25 – 1.33 Normative corundum: 2.96 – 3.69 % ΣREE: 189.1 ppm	Age: 316.6 ± 0.5 Ma (⁸⁷ Sr/ ⁸⁶ Sr) _i = 0.7151 ± 0.0009 εNd _t = -8.3 δ ¹⁸ O = 11.10 – 11.33 ‰
<i>Granite G10</i> Around the geodesic vertice of Arejadouro and at NW of Pinhal do Douro in the S. Around Castelo de Ansiães in the W.	Muscovite-dominant granite.	Medium-grained slightly porphyritic granite; (2 × 0.7 cm to 1 × 0.7 cm). Absence of enclaves.	Three distinct homogeneous bodies, two of 4 km ² and 6 km ² in the S, and a third of 0.4 km ² in the W, show a faint magmatic N60°W foliation defined by oriented feldspar phenocrysts and biotite. This granite intruded Douro Group metasediments and granite G7, and partially surrounds the early syn-D ₃ granite G4 and the granite G9, showing fault contacts. It occurs associated to NNE-SSW fault zones and it is affected by N60–70°W and N40–50° E secondary joints and strong brittle deformation. Typically, it is intensely weathered.	ASI: 1.29 – 1.34 Normative corundum: 3.27 – 3.94 % ΣREE: 64.2 ppm	Age: 316.2 ± 0.7 Ma (⁸⁷ Sr/ ⁸⁶ Sr) _i = 0.7147 ± 0.0011 εNd _t = -8.4 δ ¹⁸ O = 10.93 ‰

Table 2

Average modal compositions and average whole-rock chemical analyses in wt.% and trace elements in ppm of granites G7 – G10 from the Carrazeda de Ansiães area, northern Portugal

	G7	σ	G8	σ	G9	σ	G10	σ
Quartz	30.6	1.4	30.2	3.1	31.6	1.5	31.9	1.2
Plagioclase	31.6	2.5	27.8	2.1	29	1.6	32.4	1.8
Microcline	22.4	2	21.9	2	22.4	2.8	20.3	1.4
Biotite	5.1	0.5	9.7	2.1	6.1	0.5	2.3	0.3
Muscovite	9.8	1.8	9.7	2.2	10.3	1.1	12.5	1.1
Tourmaline	0.2	0.3	-	-	0.1	0.1	0.1	0.1
Apatite	0.4	0.1	0.5	0.1	0.4	0.1	0.6	0.2
Other	-	-	0.2	0.1	0.2	0.1	-	-
n	6		3		3		3	
 SiO ₂	72.13	0.43	69.98	1.19	71.55	0.50	73.35	0.48
TiO ₂	0.21	0.04	0.45	0.07	0.31	0.02	0.13	0.02
Al ₂ O ₃	15.01	0.31	15.47	0.35	14.86	0.24	14.80	0.12
Fe ₂ O ₃	0.48	0.11	0.68	0.17	0.48	0.11	0.38	0.08
FeO	1.03	0.11	1.76	0.31	1.31	0.10	0.67	0.05
MnO	0.03	0.01	0.03	0.00	0.03	0.00	0.03	0.01
MgO	0.40	0.06	0.76	0.15	0.50	0.04	0.23	0.03
CaO	0.65	0.06	0.82	0.07	0.72	0.03	0.51	0.03
Na ₂ O	3.50	0.21	3.06	0.20	3.19	0.15	3.69	0.16
K ₂ O	5.05	0.18	5.44	0.18	5.23	0.20	4.66	0.21
P ₂ O ₅	0.33	0.03	0.35	0.01	0.33	0.02	0.34	0.02
H ₂ O+	0.84	0.22	0.98	0.07	1.07	0.06	1.01	0.07
H ₂ O-	0.33	0.10	0.30	0.04	0.30	0.05	0.26	0.07
S	0.01	0.01	0.01	0.00	0.01	0.00	0.01	0.00
Total	100.00	0.29	100.08	0.30	99.88	0.31	99.88	0.31
O ≈ S	0.01	0.01	0.00	0.00	0.00	0.00	0.00	0.00
Total	99.99	0.29	100.08	0.30	99.88	0.31	99.88	0.31
 ASI	1.29	0.04	1.34	0.05	1.30	0.03	1.32	0.02
C	3.40	0.43	3.89	0.52	3.43	0.25	3.60	0.21
 Cl	110	0	56	9	50	0	60	10
F	1430	342	1955	78	2000	130	1673	345
Ga	21	2	24	0	23	1	22	1
Cr	34	8	38	3	40	6	32	3
V	8	2	23	6	13	1	5	1
Nb	14	2	13	1	12	1	16	1
Zn	67	16	91	10	87	7	62	6
Sn	20	3	10	2	15	2	31	4
Li	198	44	204	49	169	25	241	73
Ni	5	2	11	2	8	1	4	0
Co	3	1	7	1	5	1	3	1
Zr	73	30	201	29	140	12	53	7
Cu	4	2	10	3	5	2	5	4
Y	10	1	14	2	10	1	9	2
Sr	76	19	135	29	81	8	43	6
Pb	34	5	36	3	30	2	23	8
Ba	212	57	444	88	263	26	103	32
Rb	377	51	376	17	400	3	503	30
Cs	47	9	26	6	33	6	61	10
W	5	1	5	1	5	1	6	1
U	12	5	11	2	11	2	13	6
Th	12	6	35	4	26	2	7	3
Hf	*		5	1	4	0	*	
As	5	1	8	0	5	2	4	0
Bi	2	0	*		*		2	0
n	17		8		10		8	

G7– Medium- to coarse-grained slightly porphyritic muscovite > biotite granite; G8– Medium-grained porphyritic biotite ≈ muscovite granite; G9– Medium-grained porphyritic muscovite > biotite granite; G10– Medium-grained slightly porphyritic muscovite-dominant granite; n– number of analyses; ASI– Al/[2(Ca – 1.67P) + Na + K]; C– corundum; σ – standard deviation; - – not detected; *– below the limit of quantification.

Table 3

U-Pb data of zircon and monazite from granites G7 - G10 of Carrazeda de Ansiães area, northern Portugal

Fraction	Mineral characteristics ¹	Weight ² (µg)	U ² (ppm)	Pbt ³ (ppm)	Th/U ⁴	Pbc ⁵ (ppm)	$^{206}\text{Pb}/^{204}\text{Pb}$ ⁶	$^{207}\text{Pb}/^{235}\text{U}$ ⁷	2σ (abs)	$^{206}\text{Pb}/^{238}\text{U}$ ⁷	2σ (abs)	ρ^8	Age $^{206}\text{Pb}^*/^{238}\text{U}$ ⁷ (Ma)	2σ (Ma)	Age $^{207}\text{Pb}^*/^{235}\text{U}$ ⁷ (Ma)	2σ (Ma)	Age $^{207}\text{Pb}^*/^{206}\text{Pb}$ ⁷ (Ma)	2σ (Ma)	Disc. ⁹
<i>Granite G7 (sample GL23)</i>																			
1	Z eu lp in [2]	4.0	754	40	0.11	0.74	2125	0.41127	0.00122	0.05542	0.00012	0.80	347.7	0.8	349.8	0.9	363.6	4.0	4.5
2	Z eu lp in [7]	0.5	5638	295	0.22	9.44	1398	0.38481	0.00145	0.05233	0.00013	0.72	328.8	0.8	330.6	1.1	343.1	5.9	4.3
3	Z eu lp in [1]	0.5	1366	84	0.57	8.97	360	0.37555	0.00458	0.05166	0.00035	0.59	324.7	2.2	323.8	3.4	316.9	22.2	-2.5
4	Z eu lp b [18]	1.0	6495	313	0.10	12.50	1416	0.36022	0.00121	0.04957	0.00011	0.72	311.9	0.7	312.4	0.9	316.0	5.3	1.3
5	Z eu lp in [8]	0.5	4190	218	0.15	21.66	528	0.36269	0.00242	0.04964	0.00016	0.51	312.3	1.0	314.2	1.8	328.4	13.0	5.0
6	Mz eu eq y g [2] NA	11.0	797	186	13.56	0.36	4731	0.36715	0.00091	0.05067	0.00010	0.90	318.6	0.6	317.5	0.7	309.7	2.4	-3.0
7	Mz eu eq y g [7] NA	9.0	2330	414	9.31	0.66	8409	0.36777	0.00085	0.05061	0.00010	0.95	318.3	0.6	318.0	0.6	315.9	1.7	-0.8
<i>Granite G8 (sample GQV8)</i>																			
8	Z sb fr y in [8]	3.0	589	42	1.75	0.13	2372	0.36992	0.00134	0.05072	0.00013	0.71	319.0	0.8	319.6	1.0	324.3	5.8	5.8
9	Z eu lp in [4]	0.5	174	10	0.72	0.00	331	0.36856	0.00829	0.05026	0.00023	0.44	316.1	1.4	318.6	6.1	336.6	46.6	46.6
10	Z eu lp y in [1]	0.5	514	27	0.59	0.00	662	0.36331	0.00418	0.04982	0.00017	0.44	313.4	0.9	314.7	3.2	324.1	23.5	23.5
11	Z eu lp y in [3]	0.5	2634	135	0.33	4.28	1009	0.36176	0.00193	0.04972	0.00015	0.63	312.8	0.9	313.5	1.4	318.8	9.4	9.4
12	Z eu lp y in [1]	0.5	894	48	0.36	4.00	363	0.36676	0.00433	0.04928	0.00015	0.46	310.1	1.1	317.2	3.1	370.3	24.0	24.0
13	Z eu lp y in [f]	13.0	571	32	0.60	2.14	789	0.35925	0.00169	0.04922	0.00010	0.51	309.7	0.6	311.7	1.3	326.1	9.2	9.2
14	Mz sb eq y [1] NA	1.0	199	55	15.81	0.17	315	0.37652	0.00845	0.05182	0.00025	0.42	325.7	1.5	324.5	6.2	315.9	46.7	46.7
<i>Granite G9 (sample GC5)</i>																			
15	Z eu sp in [1]	0.5	1929	203	0.89	12.11	659	0.70285	0.00379	0.08511	0.00024	0.55	526.6	1.4	540.5	2.3	599.7	9.7	12.7
16	Z eu sp in [1]	0.5	772	77	0.12	0.00	3123	0.93128	0.00406	0.10585	0.00037	0.72	648.6	2.2	668.3	2.1	735.3	6.4	12.4
17	Z eu sp in [3]	0.5	3334	328	0.45	3.91	2500	0.77825	0.00247	0.09394	0.00024	0.83	578.8	1.4	584.5	1.4	606.6	3.8	4.8
18	Z eu lp in [4]	0.5	615	35	0.36	0.14	541	0.42120	0.00550	0.05649	0.00019	0.47	354.2	1.2	356.9	3.9	374.4	26.5	5.5
19	Mz eu eq y g [2] NA	8.0	1322	182	6.47	0.03	15200	0.36864	0.00085	0.05072	0.00010	0.93	318.9	0.6	318.6	0.6	316.5	1.9	-0.8
20	Mz eu y g [2] NA	0.5	26320	2875	4.50	9.49	6202	0.36622	0.00086	0.05043	0.00010	0.93	317.2	0.6	316.8	0.6	314.5	2.0	-0.9
21	Mz eu eq y [2] NA	1.0	5457	1055	10.55	1.93	4384	0.36555	0.00093	0.05024	0.00011	0.86	316.0	0.7	316.4	0.7	319.1	2.9	1.0
22	Mz eu eq y [4] NA	1.0	3353	735	12.03	2.79	2254	0.37033	0.00106	0.05092	0.00011	0.78	320.2	0.6	319.9	0.8	317.7	4.0	-0.8
<i>Granite G10 (sample GAJ3)</i>																			
23	Z eu lp [1]	1.0	251	13	0.39	1.31	241	0.34255	0.00684	0.04686	0.00015	0.45	295.2	0.9	299.1	5.2	329.7	41.9	10.7
24	Z eu lp [1]	1.0	575	25	0.12	0.90	577	0.32769	0.00326	0.04505	0.00015	0.45	284.1	0.9	287.8	2.5	318.1	20.2	10.9
25	Z eu lp b [4]	4.0	6570	346	0.07	18.13	1218	0.40360	0.00189	0.05394	0.00019	0.80	338.7	1.2	344.3	1.4	382.0	6.3	11.6
26	Z eu lp in [1]	0.5	3075	190	0.12	0.00	3160	0.50153	0.00195	0.06564	0.00021	0.79	409.8	1.3	412.7	1.3	429.1	5.3	4.6
27	Mz sb eq y g [1] NA	8.0	2075	422	11.11	0.19	14873	0.36783	0.00086	0.05060	0.00010	0.95	318.2	0.6	318.0	0.6	317.0	1.7	-0.4
28	Mz eu eq y g [1] NA	6.0	1044	102	3.40	0.16	7278	0.39926	0.00106	0.05496	0.00013	0.88	344.9	0.8	341.1	0.8	315.3	2.9	-9.6
29	Mz eu eq y [6] NA	3.0	7206	1182	8.34	3.66	5284	0.36533	0.00089	0.05033	0.00010	0.93	316.5	0.6	316.2	0.7	313.6	2.1	-1.0
30	Mz eu eq y g [6] NA	1.0	4788	768	8.02	4.89	2221	0.36684	0.00100	0.05046	0.00010	0.81	317.3	0.6	317.3	0.7	317.3	3.7	0.0

¹ Z – zircon; Mz – monazite; eu – euhedral; sb – subhedral; eq – equant; sp – short prismatic (length/width \approx 2 – 4); lp – long prismatic (length/width $>$ 4); fr – fragment; b – brown; y – yellow; g – green; in – inclusions; [N] – number of grains in fraction ($f > 50$ grains); non abraded (all other minerals abraded); unless otherwise specified all the zircons were clear and transparent.

^{2, 3, 5} Weight and concentrations are known to be better than 10 %, except for those near and below the ca. 1 μg limit of resolution of the balance.

³ Total Pb.

⁴ Th/U model ratio inferred from $^{208}\text{Pb}/^{206}\text{Pb}$ ratio and age of sample.

⁵ Total common Pb in sample (initial + blank).

⁶ Raw data corrected for fractionation and blank.

⁷ Corrected for fractionation, spike, blank and initial common Pb; error calculated by propagating the main sources of uncertainty; initial common Pb corrected using Stacey and Kramers (1975) model Pb.

⁸ (Rho) - Error correlation factor.

⁹ Degree of discordancy.

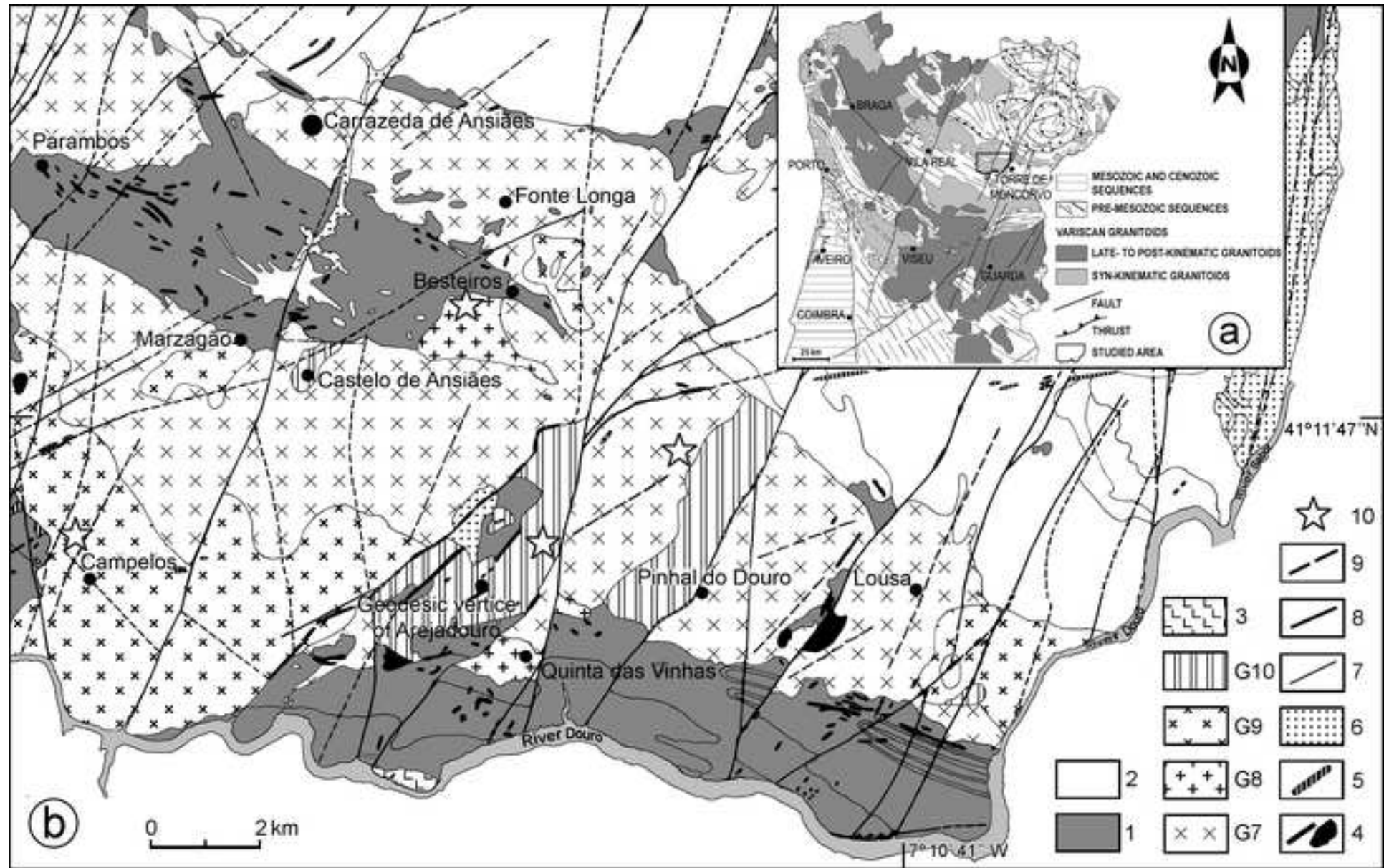


Figure 2

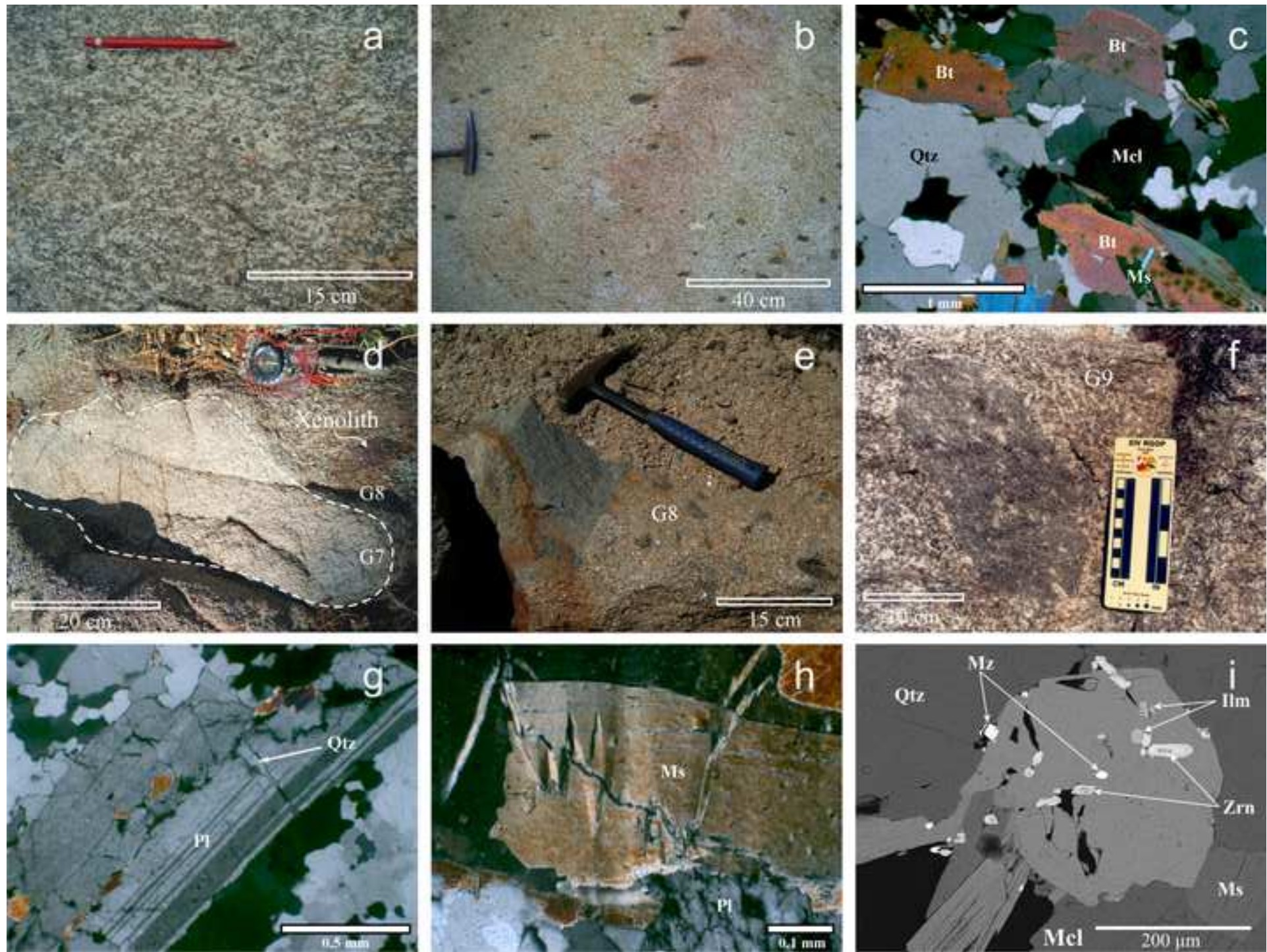
[Click here to access/download;Figure;Fig 2 JIG.tif](#)

Figure 3

Click here to access/download;Figure;Fig 3 JIG.tif

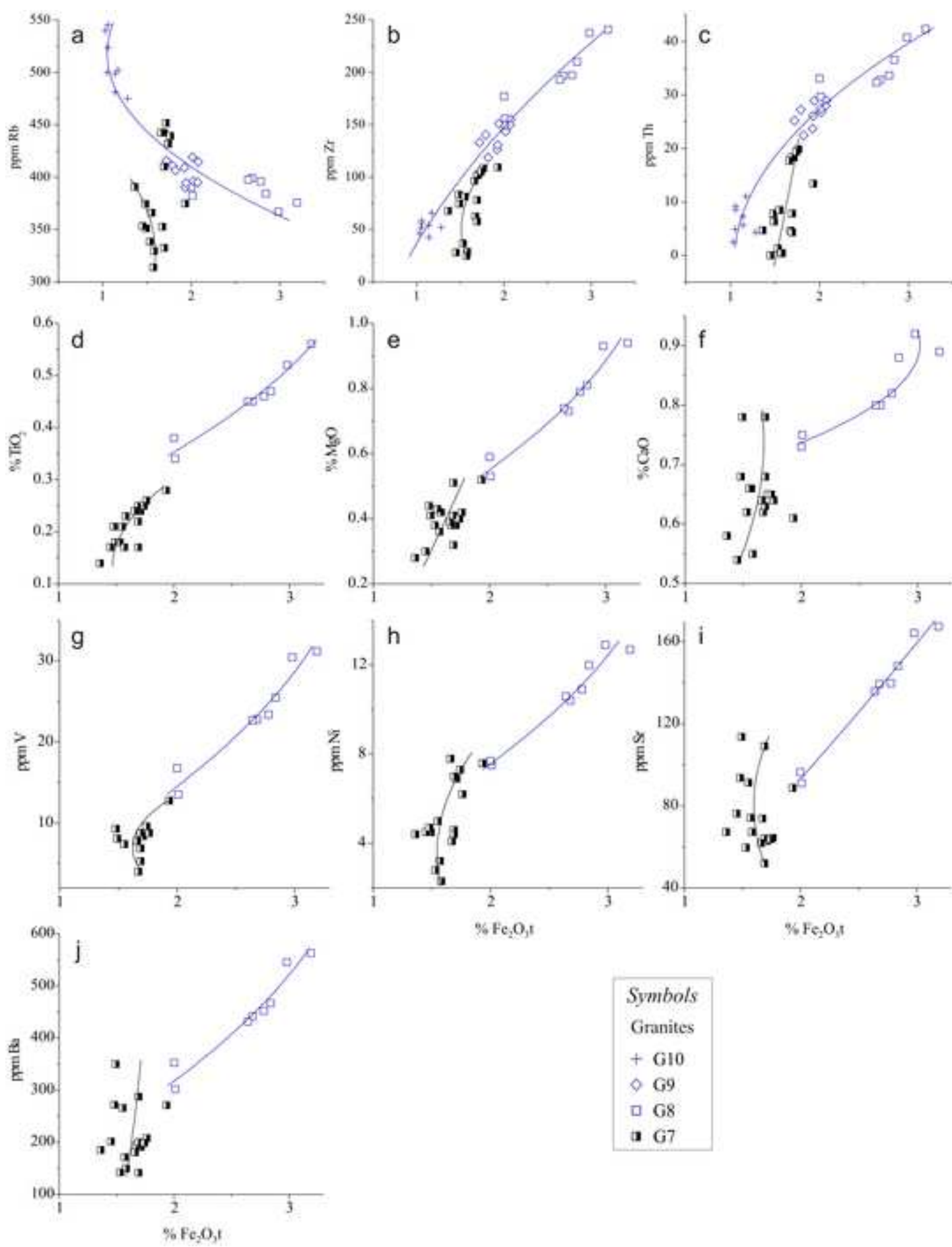


Figure 4

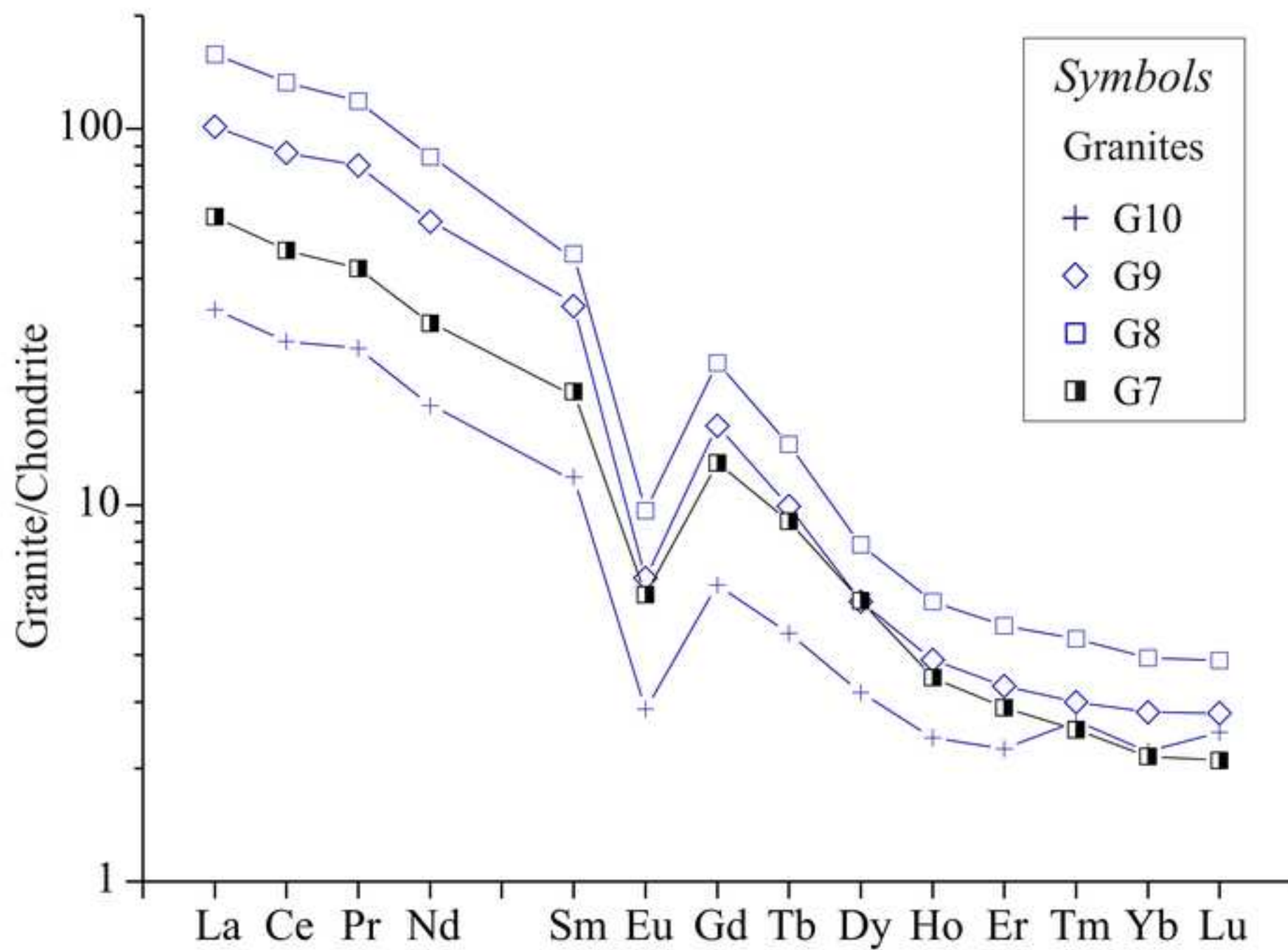
[Click here to access/download;Figure;Fig 4 JIG.tif](#)

Figure 5

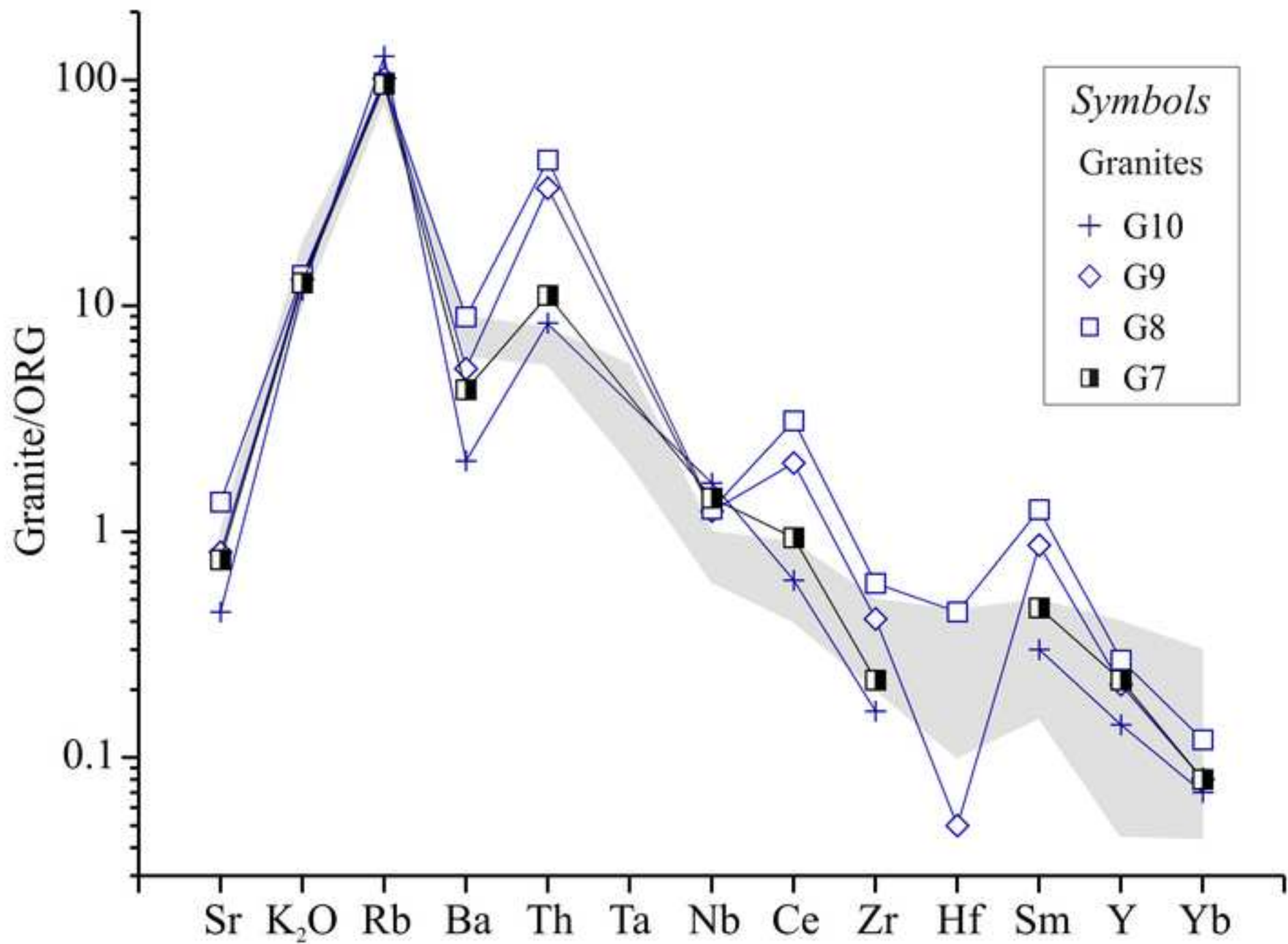
[Click here to access/download;Figure;Fig 5 JIG.tif](#)

Figure 6

Click here to access/download;Figure;Fig 6 JIG rev.tif

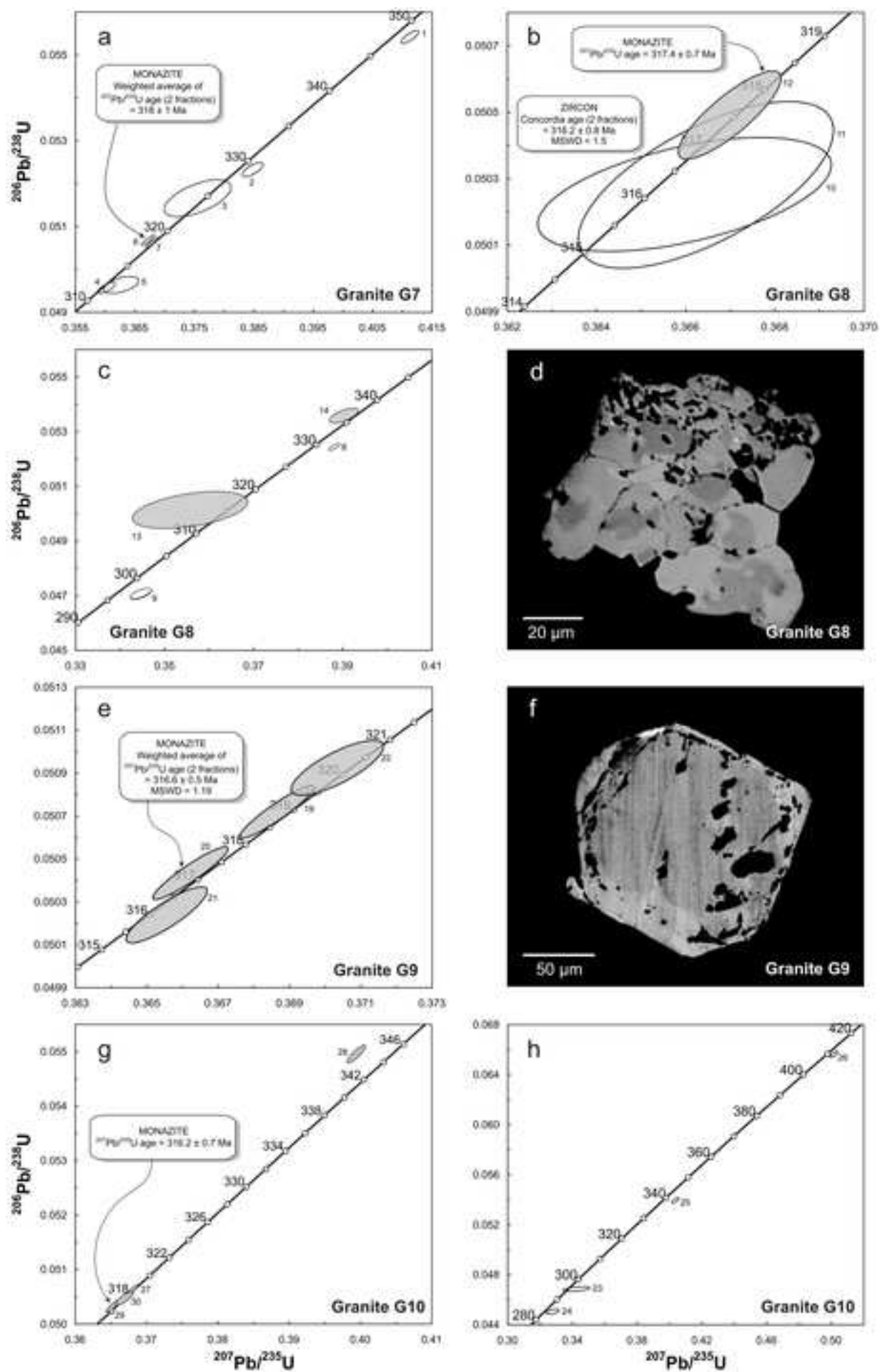


Figure 7

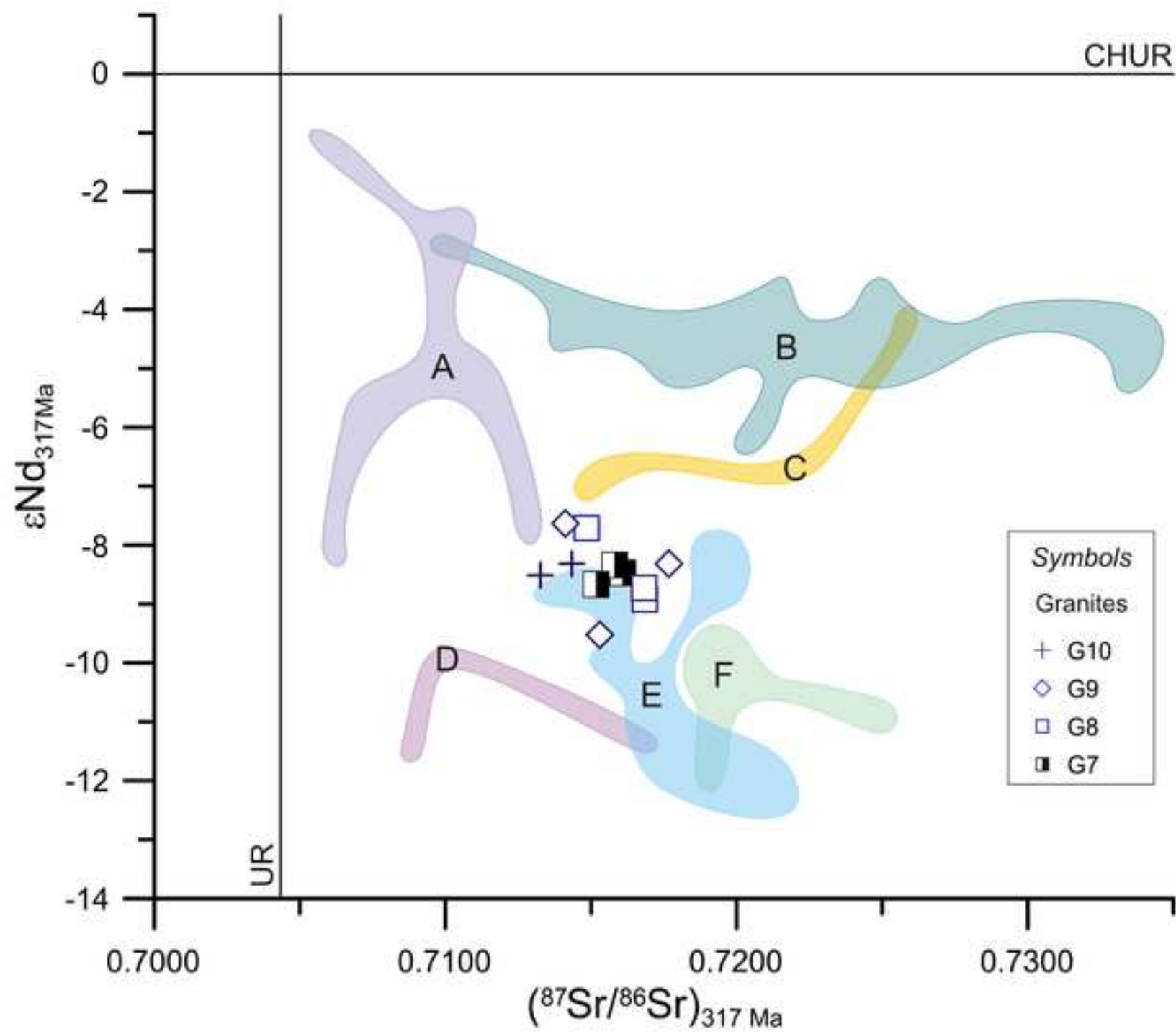
[Click here to access/download;Figure;Fig 7 JIG.tif](#)

Figure 8

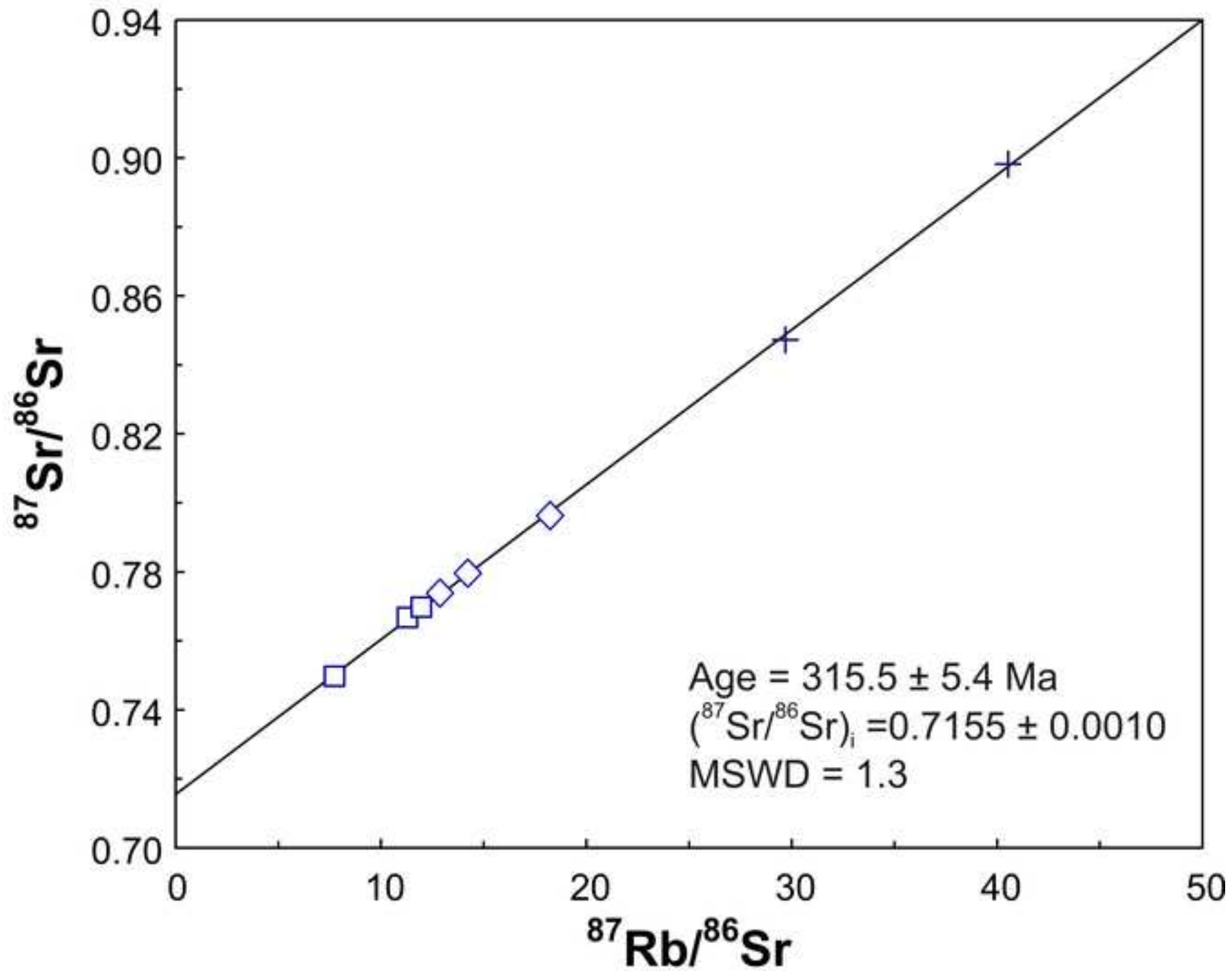
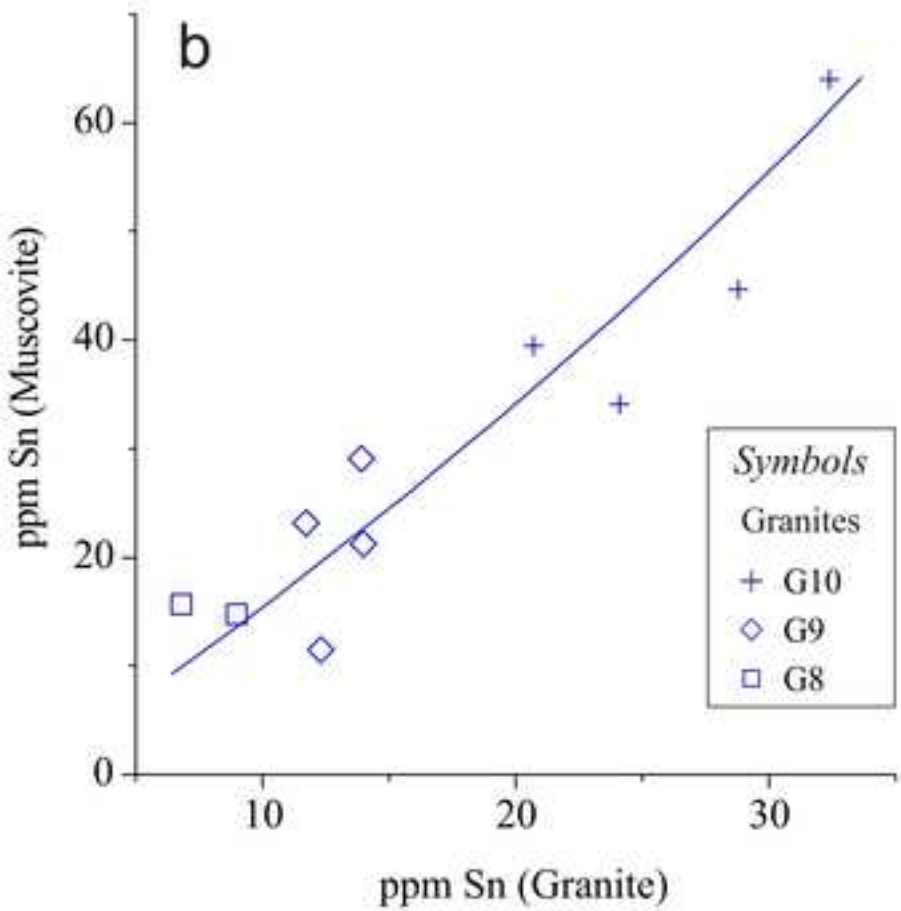
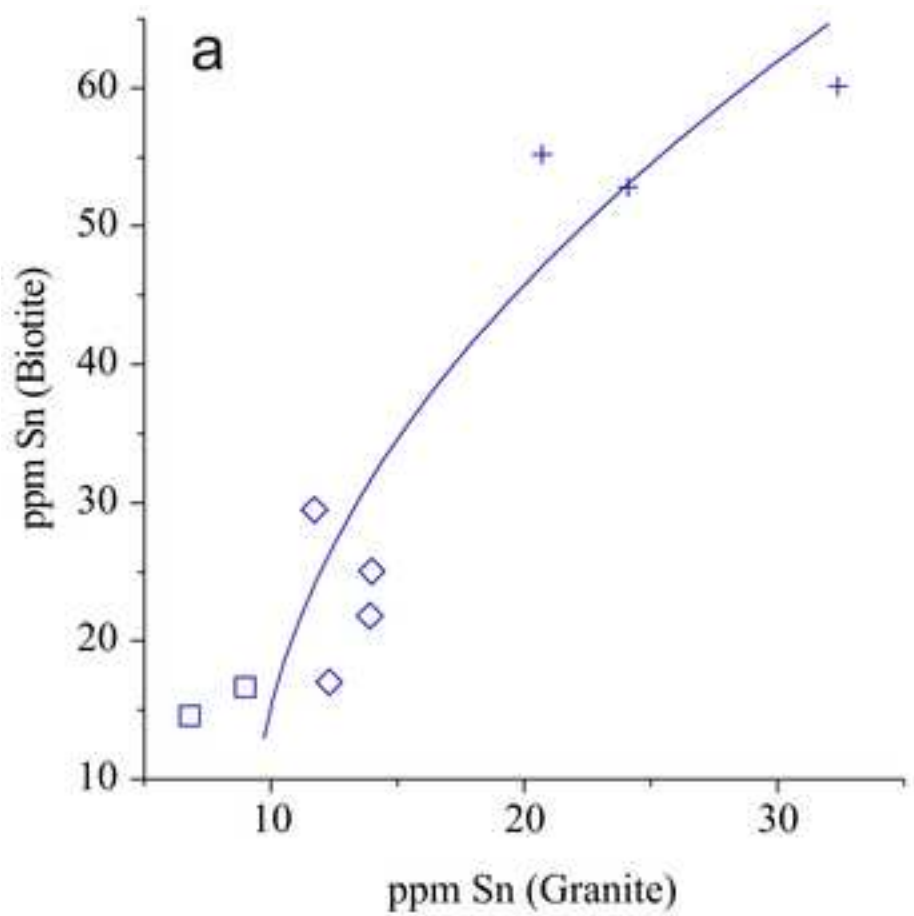
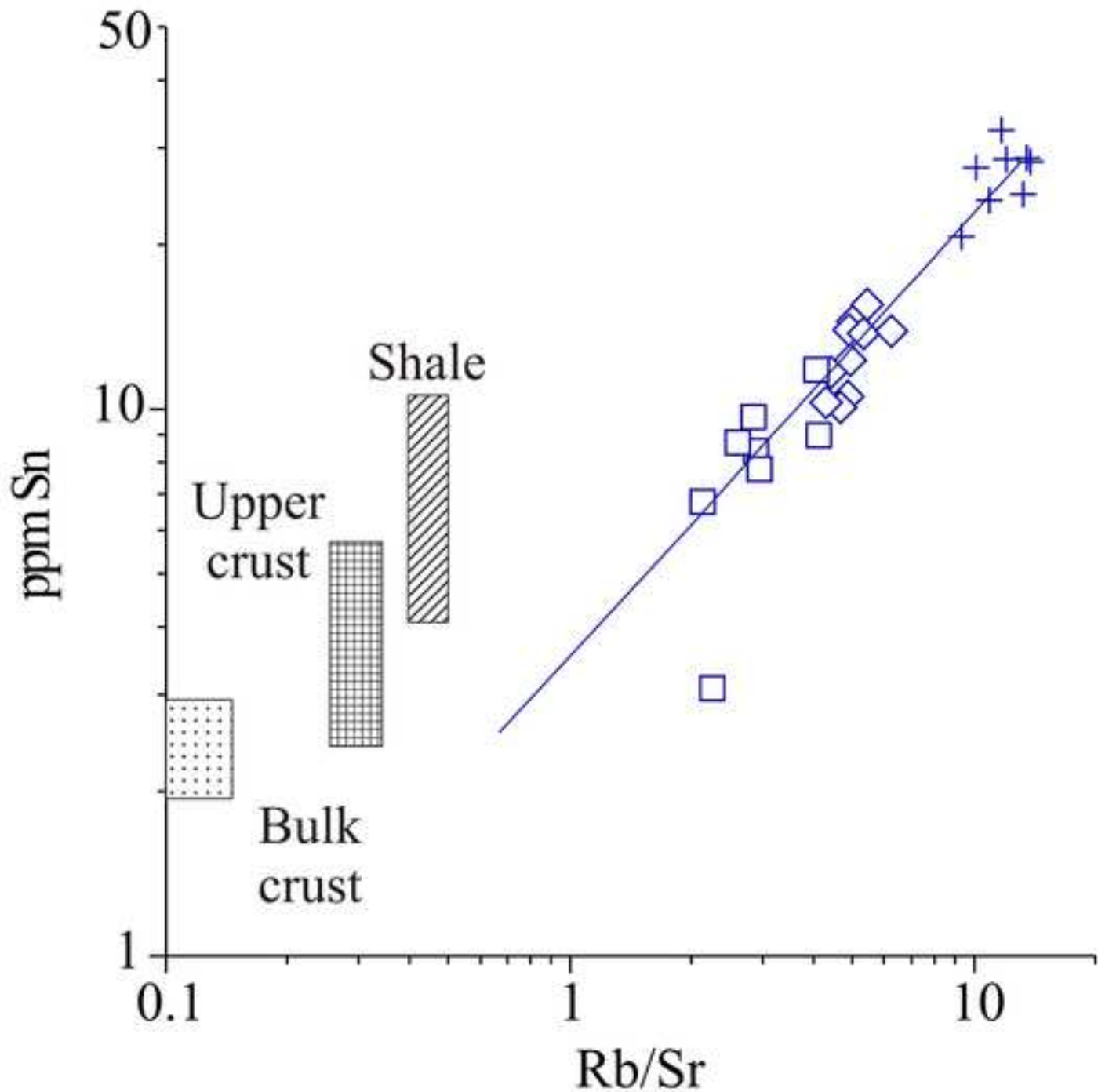
[Click here to access/download;Figure;Fig 8 JIG.tif](#)

Figure 9

[Click here to access/download;Figure;Fig 9 JIG.tif](#)





Click here to access/download
Supplementary Material
SedTable 1 rev.pdf



Click here to access/download
Supplementary Material
SedTable 2.pdf



Click here to access/download
Supplementary Material
SedTable 3.pdf



Click here to access/download
Supplementary Material
SedTable 4.pdf



Click here to access/download
Supplementary Material
SedTable 5 rev.pdf





Click here to access/download
Supplementary Material
SedTable 6.pdf



Click here to access/download
Supplementary Material

Supplemental electronic Fig. 1 JIG.tif



Click here to access/download
Supplementary Material

Supplemental electronic Fig. 2 JIG.tif



Click here to access/download
Supplementary Material

Supplemental electronic Fig. 3 JIG.tif



Click here to access/download
Supplementary Material

Supplemental electronic Fig. 4 JIG.tif